

Deformation and Fluid–Rock Interaction in the Supra-subduction Mantle: Microstructures and Water Contents in Peridotite Xenoliths from the Avacha Volcano, Kamchatka

V. SOUSTELLE^{1*}, A. TOMMASI¹, S. DEMOUCHEY¹ AND D. A. IONOV²

¹GÉOSCIENCES MONTPELLIER, UNIVERSITÉ MONTPELLIER II & CNRS, CC 60, PLACE E. BATAILLON, 34095 MONTPELLIER CEDEX 5, FRANCE

²UNIVERSITE DE LYON, UNIVERSITÉ JEAN MONNET, F42023 SAINT-ETIENNE & LABORATOIRE MAGMAS ET VOLCANS, UMR 6524, CNRS, FRANCE

RECEIVED MARCH 17, 2009; ACCEPTED NOVEMBER 11, 2009

The mantle above a subducting slab is the site of complex interactions between deformation, partial melting, fluid migration and magma transport. To constrain these interactions and their effects on olivine deformation, we analyze microstructures, crystal preferred orientations, and water contents of peridotite xenoliths entrained by andesites of the Avacha volcano, southern Kamchatka arc. These xenoliths are refractory spinel harzburgites that have coarse-grained microstructures with widely spaced subgrain boundaries and sinuous grain boundaries in olivine, consistent with deformation by dislocation creep under low deviatoric stress (≤ 13 MPa) and with a significant contribution from diffusional processes. Analysis of crystal preferred orientations (CPO) indicates dominant activation of high-temperature, low-stress $\{0kl\}$ $[100]$ slip systems in olivine and of $(100)[001]$ in orthopyroxene. In most samples, coarse opx crystals, elongated parallel to the lineation, enclose small olivine grains in crystallographic continuity with neighbouring crystals, indicating crystallization of orthopyroxene at the expense of olivine as a result of reactive percolation of Si-rich fluids coeval with the high-temperature deformation. Secondary crystallization of interstitial orthopyroxene led locally to development of opx-rich lenses parallel to the foliation, characterized by a decrease in olivine grain size and dispersion of the olivine CPO without changing the dominant slip systems. Half of the samples also show acicular orthopyroxene aggregates with which is associated a fine-grained matrix composed of rounded strain-free olivine, orthopyroxene,

spinel, and rare amphibole crystals. This matrix occurs pervasively along grain boundaries or forms millimeter-scale irregular lenses and anastomosing veinlets that crosscut the coarse crystals and their ductile deformation structures. Both acicular orthopyroxene and the fine-grained matrix are interpreted as resulting from reactive transport of H₂O-rich fluids under static conditions, probably in the lithospheric mantle. Infrared analyses show that olivine contains 1–8.6 ppm by weight of water. These low water contents are similar to those observed in spinel peridotites from other subduction zones and probably record both the low solubility of water in olivine at low pressure and dehydration during exhumation of the xenoliths. Water contents in orthopyroxene are highly variable (25–506 ppm H₂O), probably recording spatially heterogeneous interaction with fluids or melts and compositional disequilibrium in the studied samples. Change in the dominant percolation mechanism from porous flow to fracturing suggests cooling, consistent with the low temperatures estimated from pyroxene thermometry (≤ 800 – 900°C). The Avacha xenoliths therefore record pervasive deformation of a region of the mantle under asthenospheric conditions, followed by its accretion to the base of the lithosphere, probably as a result of cooling of the mantle wedge. Percolation of Si-rich fluids or hydrous melts is recorded at all stages; this probably enhanced diffusion and lowered deviatoric stresses during ductile deformation, but did not change the dominant slip direction in olivine from $[100]$ to $[001]$.

*Corresponding author. Telephone: +33-(0)467143941. Fax: +33-(0)467143603. E-mail: vsoustel@gm.univ-montp2.fr

© The Author 2010. Published by Oxford University Press. All rights reserved. For Permissions, please e-mail: journals.permissions@oxfordjournals.org

KEY WORDS: *xenolith; harzburgite; olivine; orthopyroxene; subduction; Kamchatka; microstructure; CPO; melt or fluid percolation; water; lithosphere; mantle wedge*

INTRODUCTION

The dynamics of subduction are the result of a complex force balance in which the rheology of the mantle wedge plays an essential role. The supra-subduction mantle is also the site of a series of petrological processes, ranging from dehydration of subducted material to partial melting in the wedge. Because both the presence of small melt fractions and the incorporation of water in olivine strongly reduce the strength of upper mantle rocks (Blacic, 1972; Mackwell *et al.*, 1985; Karato *et al.*, 1986; Hirth & Kohlstedt, 1995; Mei & Kohlstedt, 2000*a*, 2000*b*; Mei *et al.*, 2002; Zimmerman & Kohlstedt, 2004), the mantle wedge rheology depends on interactions between these petrological processes, migration of the resulting fluids and melts, and deformation of the solid peridotite matrix. Numerical models show that changes in mantle wedge rheology as a result of the presence of melt or water may enhance small-scale thermal convection in the wedge, leading to the erosion of the overriding arc and back-arc lithosphere (Honda *et al.*, 2002; Arcay *et al.*, 2006; Cagnioncle *et al.*, 2007; Currie *et al.*, 2008), or induce the development of partially molten diapirs in the mantle wedge (Gerya & Yuen, 2003).

Experimental studies show that incorporation of water in nominally anhydrous minerals (Hier-Majumder *et al.*, 2004; Demouchy *et al.*, 2007; Costa & Chakraborty, 2008), such as olivine, or the presence of interconnected small melt fractions also enhance diffusion, favouring recovery of dislocations (Karato *et al.*, 1993), recrystallization (Avé-Lallemant & Carter, 1970; Jung & Karato, 2001*b*), and grain growth (Karato, 1989). This is consistent with recent studies of mantle xenoliths and peridotite massifs, which suggest that melt percolation under both dynamic and static conditions may significantly modify the microstructure of mantle rocks (e.g. Vauchez & Garrido, 2001; Tommasi *et al.*, 2006, 2008; Le Roux *et al.*, 2008; Soustelle *et al.*, 2009). Reactive melt transport may also change the modal mineralogy (Le Roux *et al.*, 2007) and produce Fe- or pyroxene-enrichment, changing the density and reducing the seismic velocities of mantle rocks (Lee, 2003; Tommasi *et al.*, 2004). Finally, the presence of trace amounts of water may also result in a change of the dominant glide direction in olivine and consequently modify the crystal preferred orientations (CPO) formed during deformation by dislocation creep (Jung & Karato, 2001*a*), with direct implications for the interpretation of upper mantle seismic anisotropy in terms of flow geometry.

The actual fluids or melt content and distribution in the mantle wedge above a subduction zone and their effect on mantle wedge deformation are, nevertheless, still poorly

constrained. Direct samples of the mantle wedge are brought up to the surface by subduction-related calc-alkaline volcanism; however, these samples are extremely rare. Moreover, previous studies of subduction zone mantle xenoliths have focused on geochemical and petrological processes rather than on their deformation histories (e.g. Arai & Kida, 2000; Grégoire *et al.*, 2001; McInnes *et al.*, 2001; Arai *et al.*, 2003; Ishimaru *et al.*, 2007; Ionov & Seitz, 2008). Here we present a detailed microstructural study, including an analysis of dislocation structures, as well as measurements of crystal preferred orientations and water concentrations in olivine and orthopyroxene from 23 spinel harzburgite xenoliths from the Avacha volcano in the southeastern Kamchatka subduction zone. These data are used to investigate the relationship between deformation, fluid or melt percolation and hydration in the supra-subduction mantle.

GEOLOGICAL SETTING

All the studied xenoliths were collected from Holocene tuffs of the active Avacha (Avachinsky) volcano (53°15'N, 158°51'E; summit elevation 2741 m) located near the southeastern coast of the Kamchatka peninsula, 200 km NE of the Kurile–Kamchatka trench (Fig. 1). The Kamchatka peninsula is located in the northwestern corner of the Pacific and has been the site of continuing subduction since the Oligocene (Avdeiko *et al.*, 2002). The peninsula is composed of three volcanic fronts (Fig. 1): the older (Oligocene) Sredinny range in the west and two younger volcanic fronts in the east, of which only the easternmost is currently active (Tatsumi *et al.*, 1994). The present tectonic situation results from the collision of two volcanic arcs 5–7 Myr ago as a result of the closure of the Vetlovka basin, which separated two opposed subduction systems that were active between the middle Eocene and the Late Miocene (Konstantinovskaia, 2001). This collision resulted in an eastward displacement of the active volcanic front and the formation of the Eastern Kamchatka volcanic front, which has been active since 5 Ma (Konstantinovskaia, 2001) in response to the fast subduction (~8 cm/year) of the old Pacific plate (~80 Myr old).

Avacha is one of the most active volcanoes in the central part of the eastern volcanic front. The depths of the Moho and of the upper surface of the subducting slab beneath it are about 37 km and 120 km, respectively (Gorbatov *et al.*, 1997; Levin *et al.*, 2002). Seismic tomography shows low P-wave velocities in the mantle wedge beneath the eastern arc, which is consistent with melt generation and the locus of volcanic activity (Gorbatov *et al.*, 1999; Manea *et al.*, 2005). Seismic anisotropy measurements using local shear waves show trench-normal fast polarizations in the fore-arc and arc domains in southeastern Kamchatka (i.e. below the Avacha volcano) but trench-parallel polarizations in the back-arc (Levin *et al.*, 2004). This observation

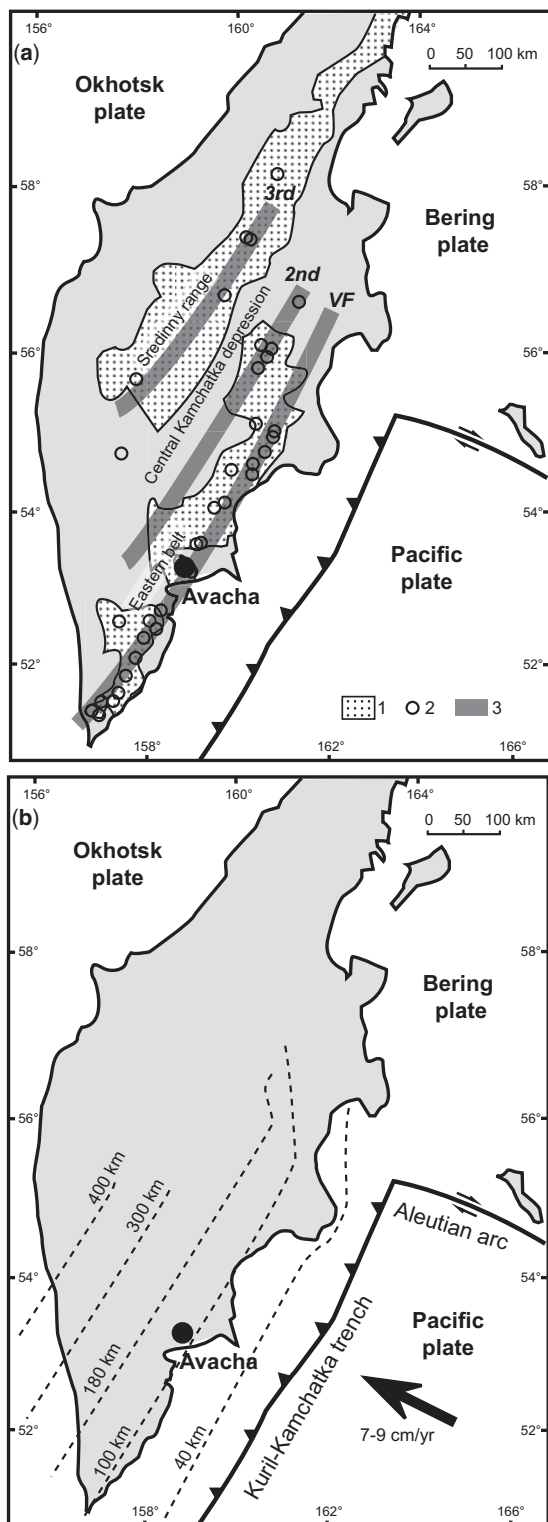


Fig. 1. (a) Simplified geological map of the Kamchatka peninsula showing the two ancient volcanic ranges (contours from Konstantinovskaia, 2001) and the active volcanic front (VF) (Tatsumi *et al.*, 1994); circles mark major active and extinct volcanoes; Avacha is indicated by a full circle. (1) Volcanic ranges, (2) active and major extinct volcanoes, (3) active and former volcanic fronts. (b) Contours of the Wadati-Benioff zone beneath southern Kamchatka (Gorbatov *et al.*, 1997; Ishimaru *et al.*, 2007).

suggests that two-dimensional corner flow in the mantle wedge does not extend inland beyond the volcanic arc (Levin *et al.*, 2004). Beyond this, the anisotropy is interpreted as recording asthenospheric flow around and beneath the disrupted slab edge at the Aleutian junction (Peyton *et al.*, 2001).

The Avacha volcano formed in the late Pleistocene, and the last eruptions occurred in 2001. Large Holocene eruptions have produced ash-falls and pyroclastic flows, with compositions varying from low-K andesite to basaltic andesite, dated using ^{14}C from 7200 to 3700 years BP (Braitseva *et al.*, 1998). The xenoliths studied here are angular blocks (10–40 cm in size) collected in volcanic ash on the western slope of the volcano (Ionov, 2009).

MODAL COMPOSITIONS AND GEOCHEMICAL DATA

All studied xenoliths are fresh peridotites with no secondary alteration. The majority (AV1 to AV17) are homogeneous at the hand-specimen scale, but some samples (AV18 to AV23) are crosscut by millimeter-scale pyroxene-rich veins or pockets. These peridotites have been the subject of a detailed petrological and geochemical study (Ionov, 2010), including petrographic descriptions and major and trace element analyses of whole-rocks and minerals. These data are summarized below. The compositions of the pyroxene-rich veins have been discussed in Bénard & Ionov (2009).

The Avacha peridotites are spinel harzburgites composed of 67–79% olivine (ol), 18–30% orthopyroxene (opx), $\leq 1\%$ spinel (sp), 1–3% clinopyroxene (cpx), and $\leq 1\%$ amphibole (amph); the mass proportions of minerals were calculated from whole-rock and mineral major oxide compositions. Cpx and amphibole are always interstitial. Coarse-grained orthopyroxenes show widespread unmixing and core–rim zoning in Ca and Al, indicating cooling from sub-magmatic temperatures to 900–1000°C. Late-stage acicular or fine-grained interstitial orthopyroxene exhibits a broad range in Ca contents, possibly as a result of cooling to ≤ 800 –900°C followed by heating shortly before the eruption. The Avacha peridotites are highly refractory, with $\geq 44\%$ MgO and very low Al_2O_3 and CaO (0.4–0.9%), TiO_2 ($\leq 0.01\%$), Na_2O ($\leq 0.03\%$), K_2O and P_2O_5 (below detection) contents in whole-rocks, high Mg-number $[\text{Mg}/(\text{Mg} + \text{Fe})_{\text{at}}]$ in olivine (0.907–0.918), high Cr-number $[\text{Cr}/(\text{Cr} + \text{Al})_{\text{at}}]$ in spinel (0.53–0.65), and very low Al_2O_3 ($\leq 2.1\%$) in orthopyroxene and Na_2O (0.1–0.3%) in clinopyroxene. These compositions are consistent with up to 30–40% of melt extraction at ≤ 1 –2 GPa, leaving no clinopyroxene in the peridotitic residue.

Compared with refractory peridotite xenoliths in continental basalts, the Avacha harzburgites tend to have

higher orthopyroxene (and SiO_2) and lower clinopyroxene contents. These features may indicate either fluid fluxing during melting in the mantle wedge or post-melting enrichment in SiO_2 as a result of reactive percolation by Si-rich fluids leading to crystallization of orthopyroxene at the expense of olivine. This silica enrichment is restricted to peridotites with abundant coarse orthopyroxenes and is not related to late-stage processes.

Abundances of rare earth elements (REE) in the Avacha peridotites are very low (≥ 10 times lower than in primitive mantle). All the studied xenoliths show depletion in the light and middle relative to the heavy REE, suggesting that partial melting was not followed by subsequent metasomatism by basaltic magma or low melting degree products.

MICROSTRUCTURAL OBSERVATIONS

Most of the studied xenoliths have coarse-grained porphyroclastic microstructures characterized by olivine and orthopyroxene crystals up to 5 mm wide (Fig. 2). These coarse porphyroclastic samples display a well-developed lineation marked by spinel trails and by the elongation of coarse olivine crystals that show aspect ratios ranging from 1:4 to 1:2 (Fig. 2a and b). Some coarse porphyroclastic xenoliths also show aligned discontinuous opx-rich lenses, up to 1 cm thick, which are characterized by finer olivine grain sizes (< 0.5 mm on average, Fig. 2a). Both coarse- and fine-grained olivine crystals have curvilinear grain boundaries that locally evolve into more polygonal shapes, forming 120° triple junctions (Fig. 2b and c). They usually display undulose extinction and widely spaced subgrain boundaries. In the coarse grains, the latter tend to be normal to the crystal elongation (Fig. 2b). An exception is sample AV3, where subgrain boundaries are parallel to the elongation of the olivine crystals. Both the orientation of the subgrains and the crystal elongation in this sample are, however, normal to the lineation marked by the spinel trails, suggesting that the elongation of the olivine crystals in this sample is a 'false' lineation formed by rotation recrystallization along (100) subgrain boundaries. Although rare, this phenomenon has previously been described in both peridotites and quartzites (Bouchez *et al.*, 1984; Tommasi *et al.*, 2001). Finally, neighbouring olivine crystals intercalated with orthopyroxene in opx-rich lenses often show similar crystallographic orientations and intracrystalline deformation features suggesting that they were originally part of a single coarse olivine crystal that was partially replaced by orthopyroxene (Figs 2e and 3). Inclusion trails crosscutting several olivine crystals are common. They may represent healed fractures.

The coarse porphyroclastic peridotites display two types of orthopyroxene. 'Coarse' orthopyroxene occurs as isolated grains or in aggregates (Fig. 2a). Grain sizes vary from 0.2 to 5 mm, but millimeter-sized grains dominate. The coarser opx crystals (> 1 mm wide) often have a turbid aspect as a result of the presence of a large amount of minute fluid inclusions (Fig. 4a). Exsolution lamellae of clinopyroxene and spinel, undulose extinction, and kink bands are common in the central parts of these large orthopyroxene crystals (Fig. 4a and c). Both isolated grains and aggregates have irregular shapes indenting and sometimes enclosing olivine crystals (Fig. 4a and c). Within an aggregate, orthopyroxene grain boundaries are straight and tend to form 120° triple junctions. Olivine relicts within large orthopyroxene crystals often show the same extinction angle as neighbouring coarse olivine crystals, suggesting that they were derived from a single coarse olivine crystal that was progressively replaced by orthopyroxene (Fig. 4a). Smaller isolated orthopyroxene crystals, ≤ 0.5 mm wide, (referred to as 'interstitial' orthopyroxenes in the following discussion) are locally observed in olivine triple junctions and along two-crystal boundaries (Fig. 4b). These smaller orthopyroxene crystals usually do not show intracrystalline deformation features.

The second type of orthopyroxene (referred to as 'acicular' orthopyroxene subsequently) is characterized by aggregates of fine-grained prismatic to acicular grains, $< 50 \mu\text{m}$ in width and $< 100 \mu\text{m}$ long, with a similar crystallographic orientation; these are probably inherited from precursor coarse orthopyroxene (Fig. 4d). Acicular orthopyroxene aggregates are 1–5 mm wide and often surround coarse orthopyroxenes and olivine crystals with 'corroded' shapes (Fig. 4c). These acicular orthopyroxene aggregates are probably equivalent to the 'recrystallized orthopyroxenes' described by Arai *et al.* (2003) from a different suite of Avacha peridotite xenoliths. Acicular orthopyroxenes are usually associated with a fine-grained ol–opx–spinel matrix made up of equant olivine and orthopyroxene crystals $< 50 \mu\text{m}$ in size (Figs 2f, h and 4c–e) with minor amounts of interstitial clinopyroxene, amphibole, oxides (Ionov & Seitz, 2008), and glass. This matrix occurs in all samples, but in variable proportions. In most samples, it occurs as thin films along olivine and orthopyroxene grain boundaries (Fig. 2e and g). However, it may also locally form large (> 1 mm) irregularly shaped pockets (Fig. 2d, f and h). Larger matrix volumes are usually observed along the opx-rich lenses parallel to the foliation or around acicular orthopyroxenes. The fine-grained matrix also fills thin anastomosing veinlets (50–500 μm wide) that crosscut coarse olivine crystals and their internal deformation features (subgrain boundaries) without any evidence of displacement (Fig. 4d). These veinlets often enclose small ($< 300 \mu\text{m}$) strain-free polygonal olivine grains with strong misorientations relative to the coarse

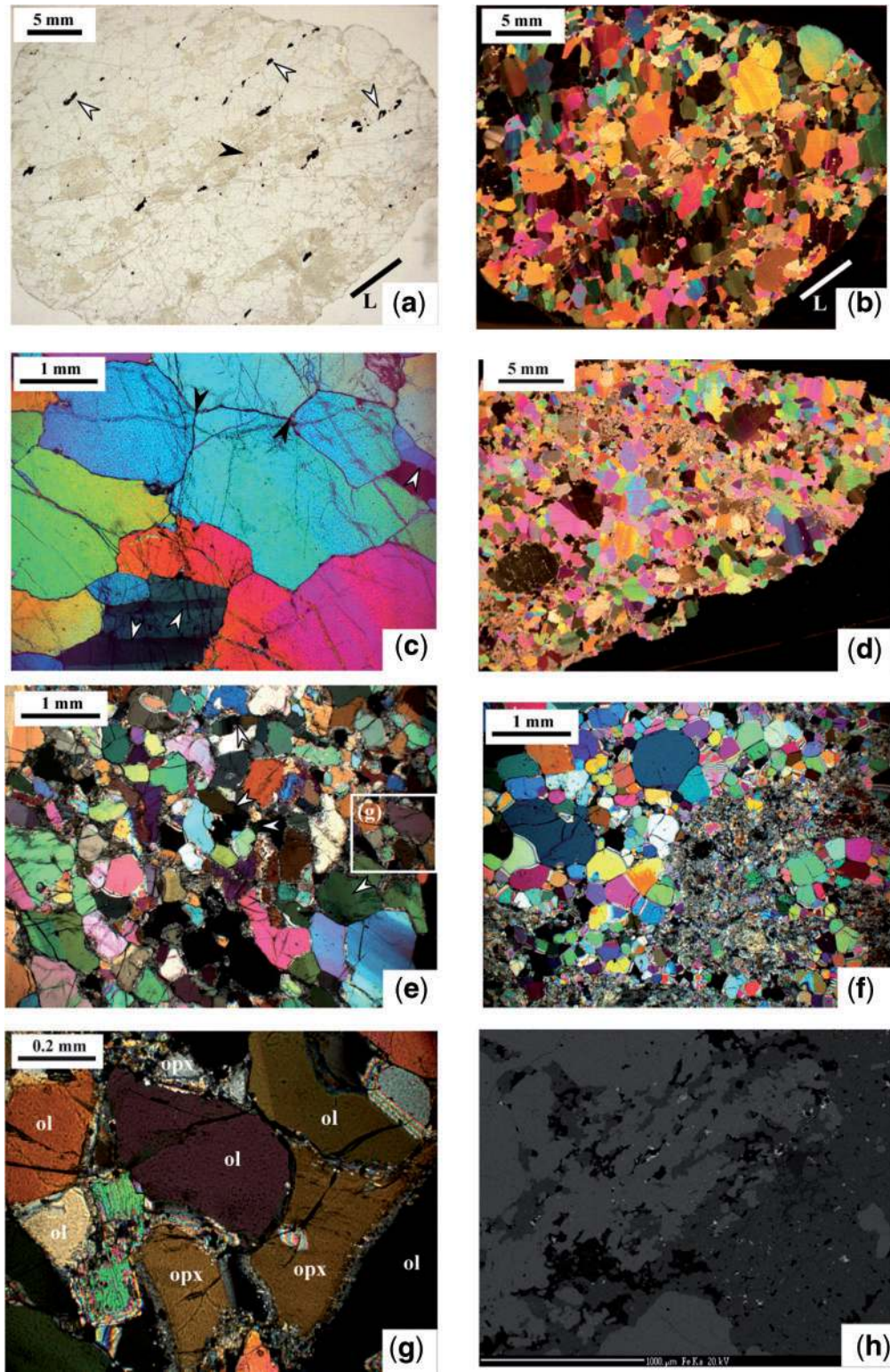


Fig. 2. Photomicrographs in plane-polarized light (a) and cross-polarized light (b–g) illustrating the typical microstructures in the Avacha peridotite xenoliths. (a) Coarse-grained peridotite AV12 showing a lineation (L) marked by the alignment of spinel (white arrows) and orthopyroxene (opx) aggregates (black arrow). (b) Same sample in cross-polarized light showing elongation of coarse olivine crystals parallel to the lineation and olivine grain refinement within opx-rich bands. (c) Subgrain boundaries (white arrow) and 120° triple junctions (black arrow) in olivine in sample AV12. (d) Fine-grained ol–opx–oxides \pm amph \pm cpx \pm glass matrix along grain boundaries and in a millimeter-scale band in sample AV5. (e) Detail of an opx-rich band in coarse porphyroclastic peridotite AV15 showing pervasive distribution of the fine-grained matrix along grain boundaries; white arrows highlight subgrain boundaries and polygonal grain boundaries in olivine. (f) Strain-free polygonal olivine and thick pocket of ol–opx–oxides \pm amph \pm cpx \pm glass matrix in equigranular peridotite AV16. (g) Detail of (e) showing interstitial orthopyroxene and thin films of the fine-grained matrix along grain boundaries. (h) Fe distribution map in the fine-grained matrix of sample AV5; scale bar represents 1mm. Olivine (light gray) is abundant in the matrix; it forms subhedral grains that appear to be in textural equilibrium with orthopyroxene (medium gray), cpx (dark gray), and amphibole (darkest gray).

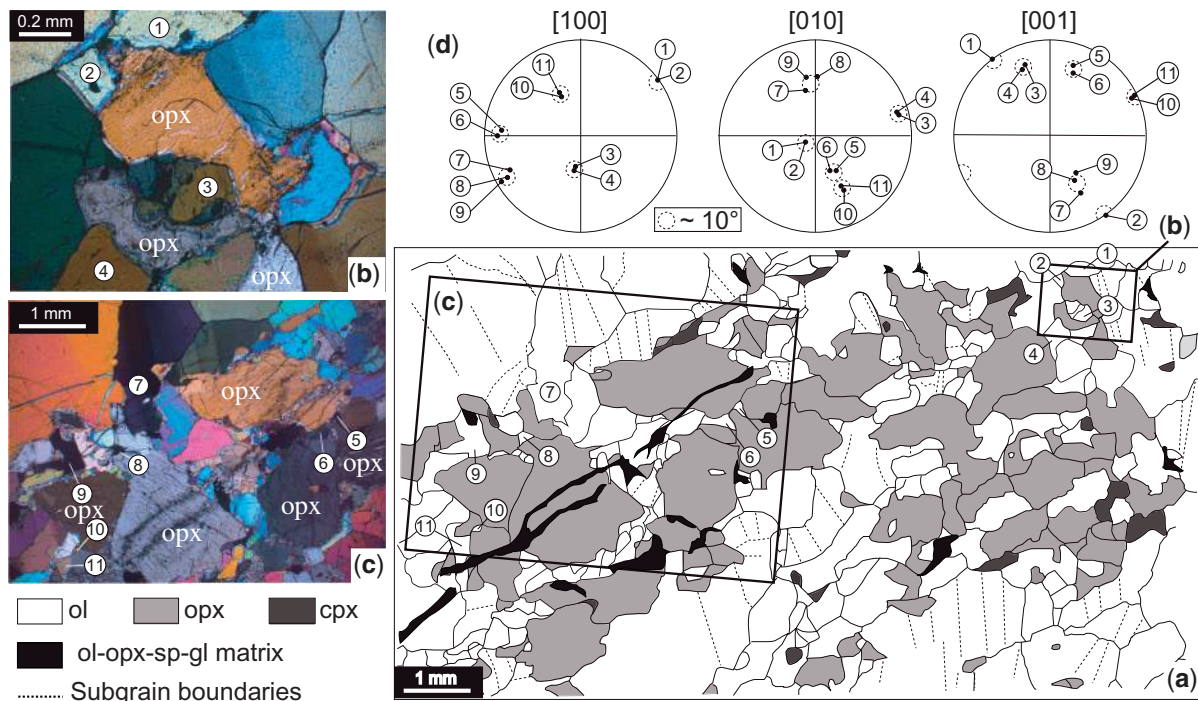


Fig. 3. Microstructure and crystallographic relations in opx-rich lenses. (a) Sketch of an opx-rich lens in sample AV12; black rectangles mark the location of cross-polarized light photomicrographs (b) and (c), which show the interstitial shapes of orthopyroxene (opx). In (c) a late vein-like structure filled by the fine-grained matrix is also observed. (d) Equal-area lower-hemisphere stereographic projections of the orientation of the [100], [010] and [001] axes of olivine crystals 1–11 in the thin-section reference frame (EBSD measurements) highlighting the crystallographic continuity between neighbouring olivine crystals separated by interstitial orthopyroxene.

host crystals (Fig. 4e). When the veinlets crosscut an orthopyroxene, they tend to lose their vein-like structure, forming diffuse reaction zones characterized by the crystallization of acicular orthopyroxene (Fig. 4d).

A single sample (AV16) has a fine-grained equigranular microstructure (Fig. 2f). The olivine crystals have polygonal shapes and are on average <0.5 mm wide. They are entirely free of intra-crystalline deformation features and often show 120° triple junctions (Fig. 2f) that may contain an isotropic phase that probably corresponds to glass. All the orthopyroxenes are acicular. This sample is particularly rich in the ol–opx–oxides ± amph ± cpx ± glass matrix, which occurs as large millimeter-scale irregular pockets (Fig. 2f).

Lastly, the coarse-grained porphyroclastic peridotites AV20 and AV21 are crosscut by linear millimeter-scale orthopyroxenite veins. These veins have a magmatic texture, characterized by equigranular strain-free orthopyroxenes (100–500 μm) with irregular shapes.

CRYSTAL PREFERRED ORIENTATIONS

Analytical procedure

Olivine and orthopyroxene crystal preferred orientations (CPO) were determined by indexation of

electron-backscattered diffraction patterns (EBSD) at the SEM-EBSD facility at Geosciences Montpellier. The EBSD patterns were generated by interaction of a vertical incident electron beam with a carefully polished thin section tilted at 70° in a scanning electron microscope (JEOL JSM 5600). The diffraction pattern was projected onto a phosphor screen and recorded by a digital CCD camera. The image was then processed and indexed in terms of crystal orientation using the CHANNEL5 software from Oxford Instruments HKL.

For each sample, we obtained crystallographic orientation maps covering almost entirely the thin section (usually 35 mm long and 20 mm wide) with sampling steps of 100, 75, or 50 μm, depending on the grain size (Fig. 5). Indexation rates in the raw maps range from 50 to 80%. In general, indexation rates are lower for orthopyroxene than for olivine. Acicular orthopyroxenes, because of the fine grain size of the crystals composing the aggregates and poor polishing, were particularly poorly indexed. Very low indexation rates (<20%) were also obtained for the fine-grained ol–opx–oxides ± amph ± cpx ± glass matrix.

Post-acquisition data treatment allowed us to increase further the indexation rate by (1) filling the non-indexed pixels that have up to eight identical neighbours with this orientation, (2) repeating this operation

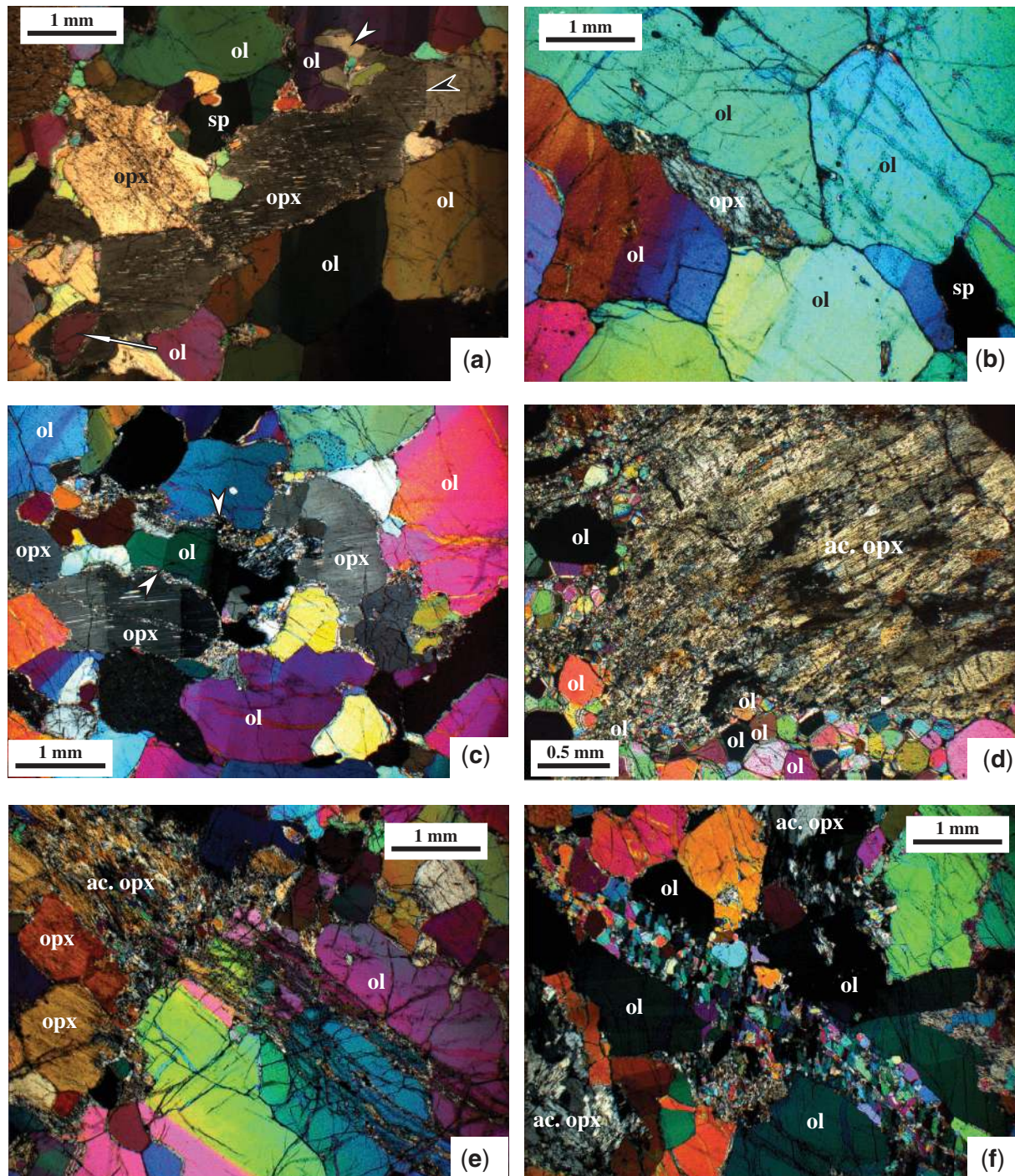


Fig. 4. Photomicrographs in cross-polarized light of typical orthopyroxene morphologies and microstructures. (a) Coarse orthopyroxene (opx) elongated parallel to the lineation with well-developed kink bands (black arrow) that fills corrosion embayments in neighbouring olivine (ol) crystals and encloses olivine relicts (long white arrow); deformation-free orthopyroxene overgrowth is marked by a short white arrow. (b) Interstitial orthopyroxene in an olivine triple junction. (c) Detail of an opx-rich band, showing corroded olivine crystals surrounded by orthopyroxene with well-developed kink bands subparallel to subgrains in neighbouring olivine as well as crystallization of the fine-grained ol-opx-oxides \pm amph \pm cpx \pm glass matrix in films along grain boundaries and in intergranular pockets (white arrows). (d) Acicular orthopyroxene (ac opx) surrounded by polygonal olivine crystals in equigranular peridotite AV16. (e) Anastomosing veinlets filled with the fine-grained ol-opx-oxides \pm amph \pm cpx \pm glass matrix in continuity with an acicular orthopyroxene in coarse porphyroclastic peridotite AV20. (f) Small polygonal strain-free olivine grains within anastomosing veinlets crosscutting intracrystalline deformation features in coarse olivine crystals in sample AV1.

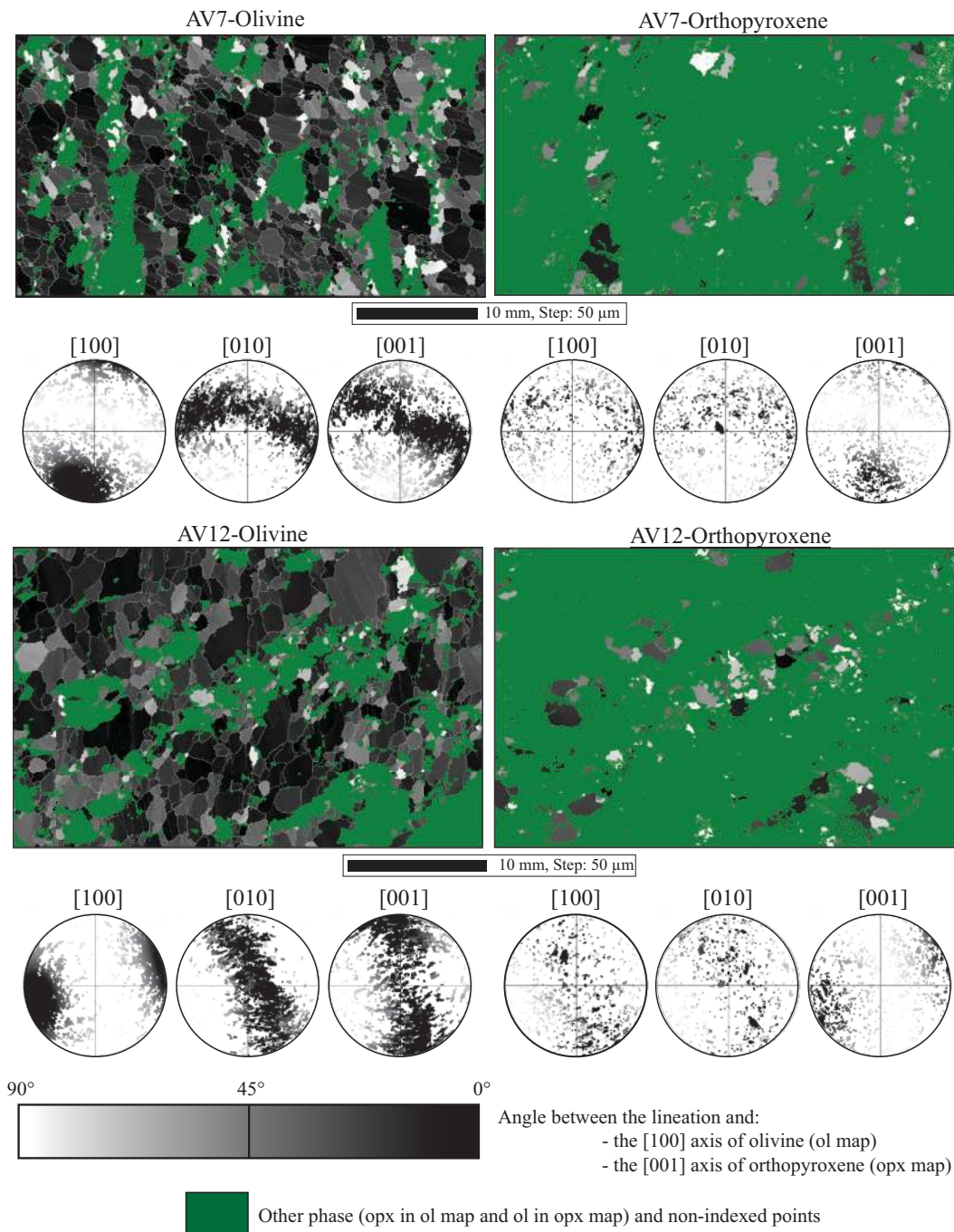


Fig. 5. Crystallographic orientation map and equal-area lower hemisphere stereographic projections in the thin-section reference frame of [100], [010], and [001] axes of olivine and orthopyroxene. Data are from samples AV7 and AV12. Greyscale in the maps indicates the angle between the orientation of the [100] olivine axis or the [001] orthopyroxene axis and the lineation indicated by the elongation of coarse olivine crystals.

using respectively seven, six, and five identical neighbours, (3) identifying the grains (i.e. continuous domains characterized by an internal misorientation $<15^\circ$), and (4) within each olivine crystal, searching and correcting for systematic indexing errors caused by the olivine hexagonal

pseudo-symmetry, which results in similar diffraction patterns for orientations differing by a rotation of 60° around [100]. At each step, the resulting orientation maps were verified by the operator to avoid over-extrapolation of the data.

Because the foliation and lineation could not be determined macroscopically in most samples, most thin-sections were cut in random orientations, rather than parallel to the lineation and normal to the foliation. To allow a straightforward comparison between the CPO of the different samples, all the CPO measurements were rotated to have the maximum concentrations of olivine [100] and [010] axes parallel to the east–west and north–south directions, respectively. When the lineation is clearly marked by the elongation of olivine or alignment of spinels, the latter is indicated in the pole figures (Fig. 6). Well-developed foliations are never observed in the studied Avacha peridotites, but when opx-rich bands are present, their average orientation is also plotted. To avoid over-representation of large crystals, CPO are plotted as one measurement per grain (average orientation of the crystal).

Results

The studied peridotites show strong olivine CPO (Figs 5 and 6). An exception is the fine-grained peridotite AV16, which has an almost random olivine CPO. Olivine CPO shows well-developed axial [100] patterns characterized by a strong point concentration of [100] axes. When observed, the mineral lineation is always sub-parallel to the maximum concentration of the olivine [100] axes (Fig. 6). [010] and [001] axes show girdle distributions normal to the [100] maximum, with two weak maxima roughly normal to each other. The [010] maximum is usually stronger than the [001] one, but this relation is reversed in samples AV10, AV11, AV18 and AV23 (Fig. 6).

The CPO strength or intensity can be defined by two dimensionless indices, as follows.

- (1) The *J* index, which is the volume-averaged integral of the squared orientation densities (Bunge, 1982). It has a value of unity for a random CPO and tends to infinity for a single crystal, but most natural peridotites show *J*-index values between two and 20, with a peak around eight (Ben Ismail & Mainprice, 1998; Tommasi *et al.*, 2000). The *J* index of all samples was calculated for both the full orientation dataset from the EBSD maps and the mean orientation for each grain using the SuperJ7x program by D. Mainprice with a 10 degree Gaussian half-width, data at 1 degree bins, and truncation of the orientation distribution function (ODF) at degree 22.
- (2) The *M* index (misorientation index), which corresponds to the difference between the observed distribution of uncorrelated misorientation angles and that predicted for a random fabric (Skemer *et al.*, 2005). It has a value of zero for a random CPO and unity for a single crystal.

J and *M* indices show a good linear correlation ($R^2=0.88$, Fig. 7), indicating that both indices correctly represent the CPO strength of the studied samples. Because most published CPO data for natural peridotites and experimental aggregates have their strength expressed as *J* indices, we chose to use this index in the following discussion as it is widely used not only in geology, but also in material sciences.

In the studied peridotites, the *J* index ranges between 9.5 and 2. This variation in *J* index is correlated with the olivine grain size distribution (Fig. 8a). The lowest *J* index is observed in the fine-grained equigranular peridotite AV16. In the coarse porphyroclastic samples, two behaviours can be discriminated: samples with >10% vol. of fine-grained olivine (<0.5 mm) show weak olivine CPO ($J < 5$), whereas the remaining samples have *J* indices between 5 and 10. These two groups may also be distinguished on the basis of their modal composition: weak olivine CPOs are associated with an enrichment in orthopyroxene (Fig. 8b). Within a group, no clear correlation between *J* index and fine-grained olivine or orthopyroxene contents can be established. Analysis of the *J* indices calculated for different grain size populations in a sample (Fig. 9) shows, however, that fine (<0.5 mm) and intermediate-size grains (0.5–1 mm) have lower *J* indices (i.e. more dispersed orientations) than coarse olivine crystals in a sample. The fine-grained population has therefore a strong influence on the estimation of the sample *J* index if the latter is calculated using one measurement per grain, as fine grains are more numerous on a given analysed surface. Comparison of *J* indices calculated using one measurement per grain and using the full orientation dataset from the EBSD map that take into account the surface of the crystals shows that the former method underestimates the intensity of the CPO (Fig. 10). This observation highlights the problem of estimating the CPO intensity in samples exhibiting strong grain-size heterogeneity. The use of one average orientation per grain overestimates the contribution of the fine grains, whereas by using the EBSD map data a higher weight is given to coarse grains. The choice depends on the type of study performed. Use of one measurement per grain allows relation of the CPO to the microstructure, as in the present study, whereas surface-weighted CPO should be preferred when calculating CPO-induced anisotropy of physical properties.

The symmetry of the olivine CPO may be defined by the relative proportion of point, girdle and random components for each axis distribution (Fig. 11). This diagram is constructed using the eigenvectors of the orientation matrix for each crystallographic axis (Vollmer, 1990). The weak CPO of the equigranular peridotite AV16 is expressed by a dominant random component in all three axes distribution. In contrast, coarse-grained porphyroclastic peridotites show a variation in the [100] and [010]

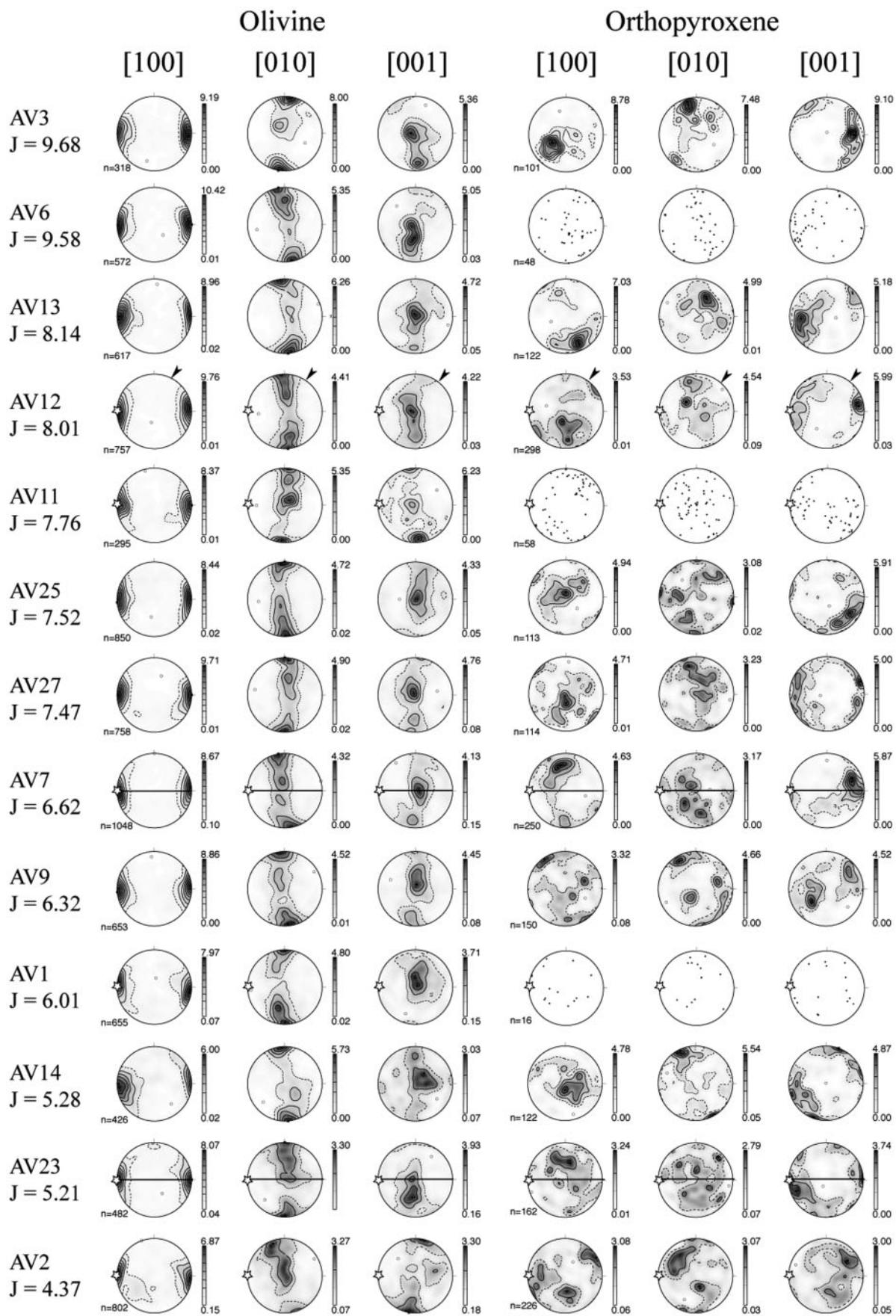


Fig. 6. Olivine and orthopyroxene crystal preferred orientations. Lower hemisphere, equal-area stereographic projections, contours at one multiple of uniform distribution. All data were rotated to have the olivine [100] maximum in the east–west horizontal direction and the [010] maximum close to the north–south horizontal direction. N, number of measured grains. Orthopyroxenes were not contoured when fewer than 100 grains were measured. Lineation, when observed, is marked by a star; when parallel to the projection plane, it is marked by a black arrow showing the circle of the pole figure.

Downloaded from https://academic.oup.com/petrology/article/51/1/1-2/3631465322 by guest on 21 August 2022

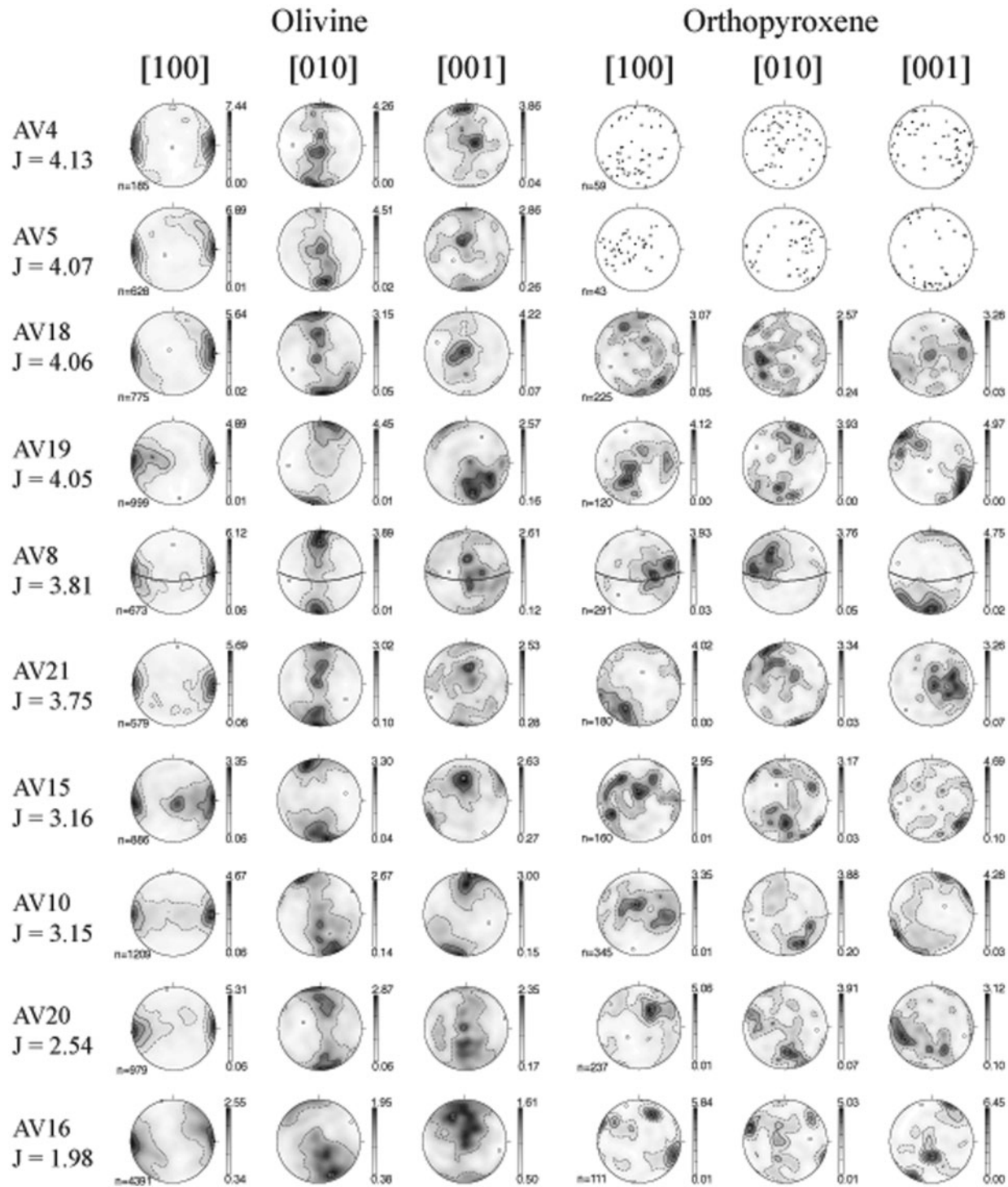


Fig. 6. Continued.

distributions symmetry with increasing proportion of fine-grained olivine crystals (Fig. 11). This evolution is correlated with a decrease in the J index. The $[100]$ distribution evolves from point symmetry towards a weak girdle

(points plot at the transition between the random and the girdle fields). The $[010]$ distribution evolves from girdle symmetry to random. Except for AV2, which has a stronger concentration of $[001]$ than of $[010]$, all samples show a

higher dispersion of [001], characterized by a dominant random component. Together, these observations show that the olivine CPO evolves from a strong axial [100] pattern to a weak orthorhombic pattern with increase in the volume of fine grains.

In most studied peridotites, orthopyroxene CPO is more dispersed than the olivine CPO (Fig. 6). The multiple maxima observed in some pole figures result from the poor indexation of orthopyroxene during the automatic mapping. Because of bad polishing or reaction rims, many large orthopyroxene crystals were incompletely indexed and were recorded in the maps as multiple isolated

patches with a similar orientation. This leads to an over-representation of the weight of this orientation and hence to a maximum in the pole figure when the latter is plotted as one measurement per grain. The same problem occurs with the acicular orthopyroxene aggregates, which form large areas with similar orientations that are very poorly indexed because of their fine-grained nature. The real orthopyroxene CPO patterns are thus partially obscured by these indexation problems, but the major features remain visible. The [001] distribution is usually characterized by a single or double maximum with, in some samples, a tendency to form a weak girdle normal to [100]. Ten samples have a maximum concentration of the orthopyroxene [001] axes close to the olivine [100] axes maximum (AV3, AV4, AV6, AV7, AV9, AV11, AV12, AV13, AV18, AV23), but with a systematic angular shift (<math><30^\circ</math>) (Fig. 6). Another 10 xenoliths have the orthopyroxene [001] maximum that differs by more than

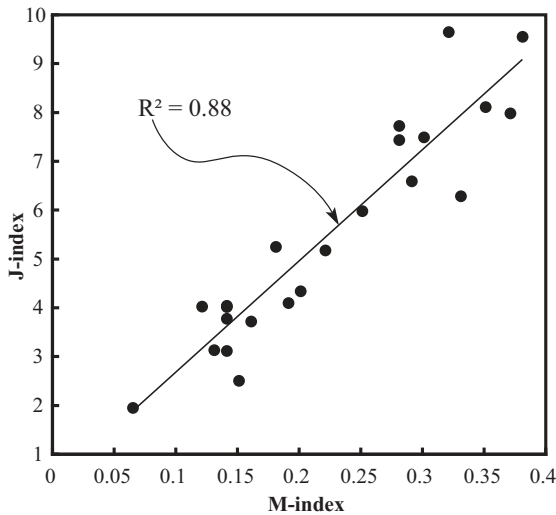


Fig. 7. Strength of olivine crystal preferred orientation in the studied samples characterized by the J and the M indices (see text for definitions). The high correlation coefficient (R^2) indicates that these two measures of the CPO strength are consistent.

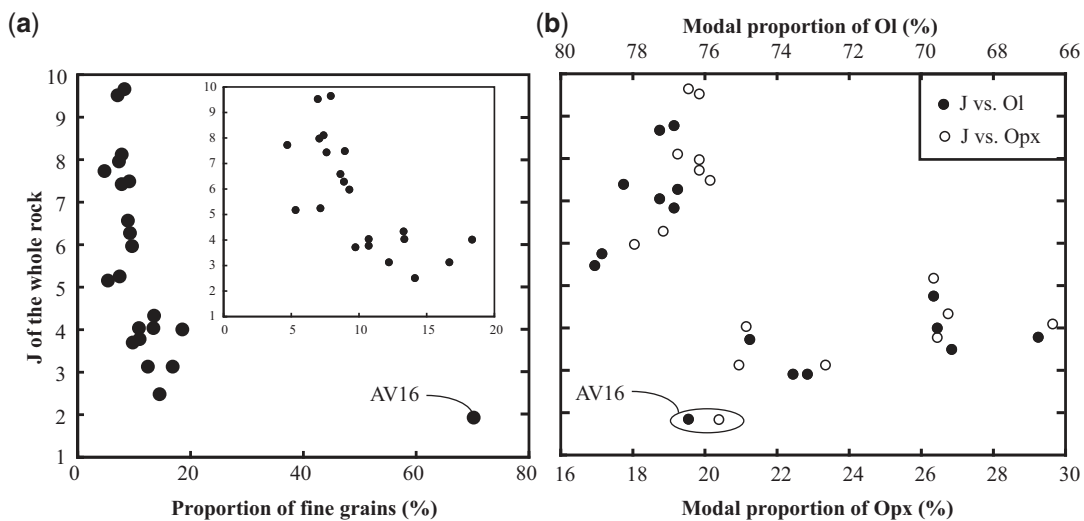


Fig. 8. J index for olivine calculated using one orientation datum per grain versus (a) the proportion (vol. %) of fine-grained olivine ($\phi < 0.5\text{ mm}</math>) and (b) the modal proportion of olivine and orthopyroxene in each sample.$

Deformation mechanisms and dominant slip systems in olivine and orthopyroxene

The well-developed olivine and orthopyroxene CPO imply that the coarse-grained Kamchatka peridotites deformed mainly by dislocation creep. Under pressure and temperature conditions appropriate to the upper mantle, the dominant slip system in orthopyroxene is (100)[001] (Doukhan

et al., 1986). Olivine deforms essentially by slip on the {0kl}[100] and {hk0}[001] systems; the relative strength of these systems depends on the temperature, pressure, deviatoric stress, and water fugacity conditions that prevail during deformation (Durham *et al.*, 1977; Mackwell *et al.*, 1985; Bai *et al.*, 1991; Jung & Karato, 2001a; Couvy *et al.*, 2004; Jung *et al.*, 2006; Raterron *et al.*, 2007).

The correlation between shape and crystal preferred orientation is a reliable tool to constrain the dominant slip systems in olivine and orthopyroxene, as these minerals display few slip systems with highly variable strengths. This results in alignment of the dominant slip direction with the shear (or maximum stretching) direction and of the normal to the slip plane with the normal to the shear plane (or foliation) in simple shear (or pure shear) deformation (Zhang & Karato, 1995; Tommasi *et al.*, 1999;

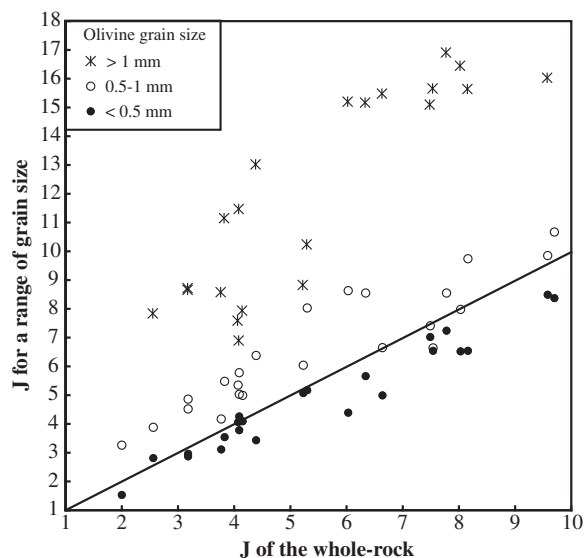


Fig. 9. J index for various olivine grain size populations vs J index of the whole-rock. Stars, coarse grains ($\phi > 1$ mm); open circles, intermediate grains (ϕ between 1 and 0.5 mm); black circles, fine grains ($\phi < 0.5$ mm).

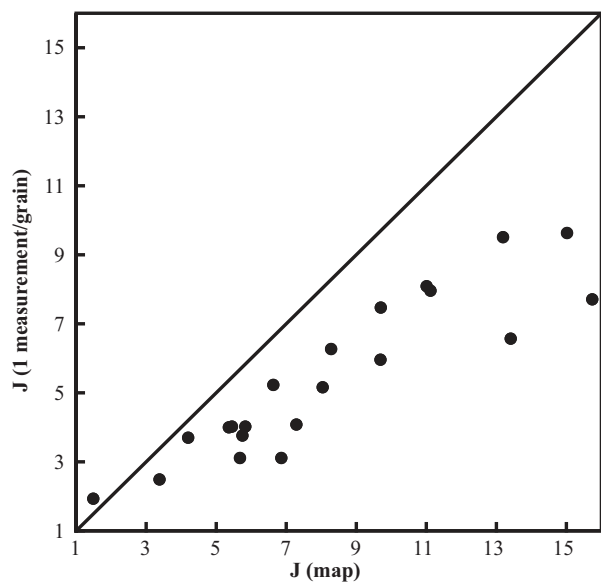


Fig. 10. Comparison of the olivine J index calculated using the raw crystallographic data from the EBSD maps with that for one orientation datum per grain.

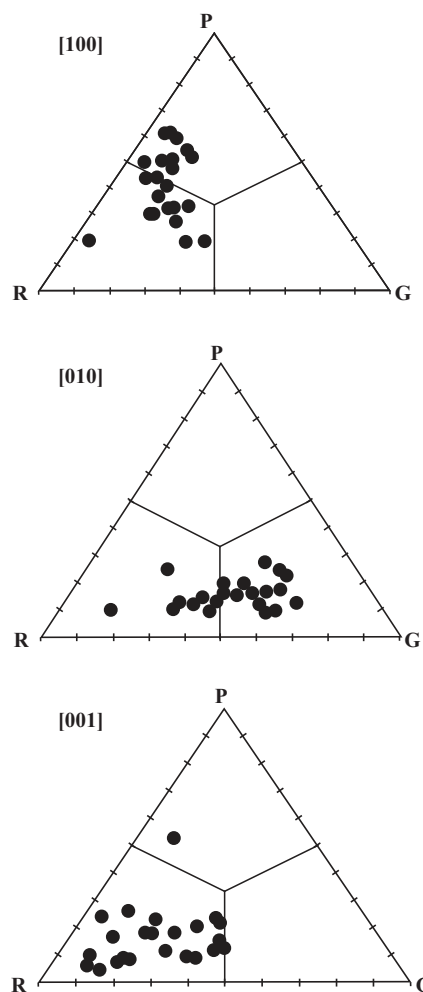


Fig. 11. Olivine CPO symmetry expressed as the proportion of point (P), girdle (G) and random (R) components calculated from the eigenvalues ($\lambda_1, \lambda_2, \lambda_3$) of the normalized orientation matrix for the three principal crystallographic axes: [100], [010] and [001]. $P = \lambda_1 - \lambda_3$, $G = 2(\lambda_2 - \lambda_3)$, $R = 3\lambda_3$.

Bystricky *et al.*, 2000). In xenoliths, however, the foliation and the lineation cannot always be easily identified and other observations are needed to constrain the dominant slip system. In this case, information on the active slip systems may be derived from the analysis of the following factors.

- (1) The relative concentrations of the three main crystallographic axes in agreement with polycrystal plasticity modelling of CPO evolution that shows that the slip direction and the normal to the plane of the dominant slip system tend to orient faster than the remaining crystallographic axes (e.g. Tommasi *et al.*, 2000).
- (2) The relations between the olivine and orthopyroxene CPO.
- (3) The rotation axes accommodating low-angle (<15°) misorientations within a crystal, because variations in crystallographic orientation within a grain or across a low-angle grain boundary (subgrain boundary), as well as the orientation of subgrain boundaries, are directly related to the dislocations forming the boundary (Frank & Read, 1950; Amelinckx & Dekeyser, 1959). Misorientation axes data should nevertheless be used with caution, as the dislocations stacked in the subgrain boundaries may not be representative of the most mobile and, hence, most active slip systems.

In all coarse-porphroclastic xenoliths, olivine displays a well-developed axial [100] pattern (Fig. 6) characterized by a strong point concentration of [100] axes subparallel to the lineation, when the latter can be observed, and systematically normal to the average orientation of the subgrain boundaries. This indicates that [100] is the dominant slip direction for olivine. This interpretation is corroborated by the predominance of (100) subgrain boundaries in the crystallographic orientation maps (Fig. 5).

Dominant [001] slip in orthopyroxene is in agreement with the observations that in most coarse-grained peridotites, orthopyroxene [001] axes are more concentrated than [100] or [010] and that in half of the studied xenoliths the orthopyroxene [001] maximum is at a low angle to both the lineation and the olivine [100] axes (Fig. 6). The poor orientation of orthopyroxene [100] and [010] axes hinders a clear determination of the slip plane, but there is a predominance of [010] rotation axes for low-angle misorientations (5–15°) in orthopyroxene crystals that is consistent with subgrain boundaries formed essentially by (100)[001] edge dislocations (Fig. 12).

Obliquity between the olivine and the orthopyroxene CPO is common in naturally deformed peridotites (e.g. Tommasi *et al.*, 2004, 2006; Le Roux *et al.*, 2008). It is usually interpreted as resulting from lower finite strains in stronger orthopyroxene crystals (Mackwell, 1991)

at a given macroscopic strain. Many Avacha peridotites, however, display an obliquity between the olivine and orthopyroxene CPO that is too strong (>20°) to result from variations in finite strain between the two minerals. We propose that this obliquity results from late to post-kinematic crystallization of part of the orthopyroxenes. This process may also explain the higher dispersion of the orthopyroxene CPO relative to the olivine CPO.

The girdle distribution of olivine [010] and [001] axes suggests activation of multiple {0kl} slip planes. The foliation is poorly developed in the studied peridotites. To determine the dominant slip plane, we therefore analyzed: (1) the relative concentrations of olivine [010] and [001] axes, represented by the ratio between the maximum

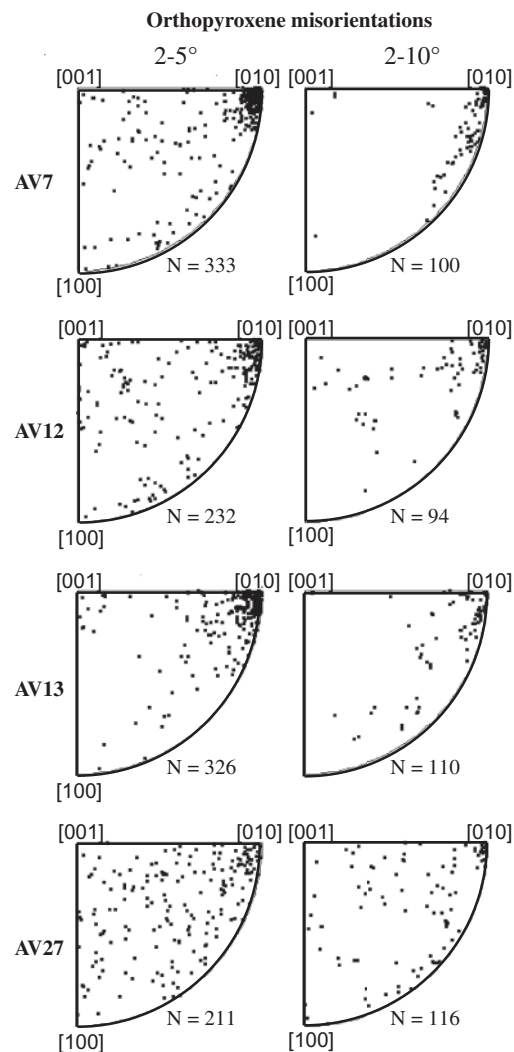


Fig. 12. Rotation axes accommodating misorientations $\leq 10^\circ$ within orthopyroxene crystals in an EBSD map. Inverse pole figures in the crystal reference frame. N, number of measurements. Predominance of [010] rotation axes is consistent with dominant activation of the [001](100) slip system.

concentration of these two axes; (2) the rotation axes (in the crystal frame) accommodating low-angle misorientations ($<10^\circ$) within olivine crystals; (3) the relative orientations of orthopyroxene [100] and olivine [010] and [001] axes for the nine samples where the slip directions of orthopyroxene and olivine were subparallel.

Analysis of Figure 13 highlights that these three independent criteria do not always provide consistent information. Most samples show a stronger concentration of [010], suggesting dominant slip on the (010) plane. However, [010] and [001] have similar concentrations in samples AV2, AV9, AV25, and AV27, suggesting equal activation of the two planes. Finally, in samples AV10, AV11, and AV18 the stronger concentration of [001] implies dominant glide on (001). On the other hand, comparison between olivine and orthopyroxene CPO highlights that sample AV18, similarly to AV7, AV12, AV13, and AV23, has the olivine [010] maximum subparallel to the orthopyroxene [100] maximum, implying dominant glide on the (010) plane. In contrast, in samples AV3, AV19, AV25, and AV27, the comparison between olivine and orthopyroxene CPO favours dominant glide on the (001) plane.

Analysis of lattice rotations across all low-angle boundaries in olivine within a map (Fig. 13) highlights that the rotation axes are mainly normal to [100], with two maxima parallel to [001] and [010]. Predominance of rotation axes close to [010] indicates a higher density of [100](001) edge dislocations in the subgrain boundaries, even in those samples where the analysis of the two other criteria clearly indicates dominant slip on [100](010).

We also compared the olivine and orthopyroxene CPO with the orientation of the opx-rich lenses when the latter were present (Fig. 5). The opx-rich lenses always contain the olivine [100] and the orthopyroxene [001] maximum concentrations. They are normal to the olivine [010] maximum concentration in sample AV7 and to the [001] maximum in AV12, suggesting dominant slip of [100] dislocations on the (010) plane in the former and on the (001) plane in the latter. However, both samples show girdle distributions of [010] and [001], suggesting that multiple $\{0kl\}$ planes were activated. In conclusion, all the observations converge towards activation of multiple [100] $\{0kl\}$ slip systems in olivine, with predominance of (010) or (001) planes depending on the sample.

DISLOCATION STRUCTURES

Sample preparation and analytical procedures

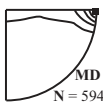




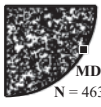
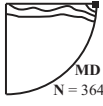

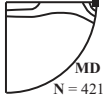
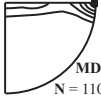
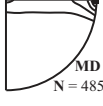
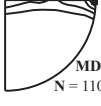
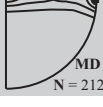
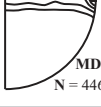
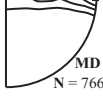
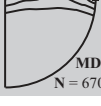
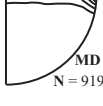
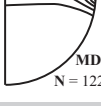
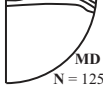

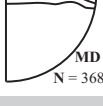
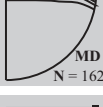
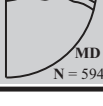
To observe the dislocation structures, sections of three coarse porphyroclastic peridotites and of the equigranular peridotite were decorated using the method described by Kohlstedt *et al.* (1976b). This method consists in annealing

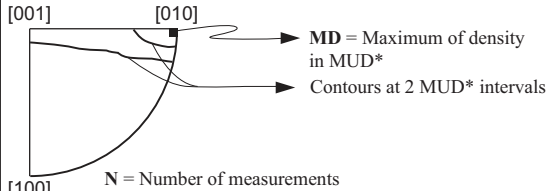
a polished sample slab for 30 min in air at 900°C (oxidizing conditions). A standard $30\ \mu\text{m}$ thin section is prepared with the previously polished face in contact with the glass slide. Observations were made using both an optical microscope in natural light and a scanning electron microscope (SEM). Electron backscattered images were obtained using a FEI Quanta 200 SEM at the acceleration voltage of 15 kV and currents up to $2\ \mu\text{A}$ in a low-vacuum chamber. Under these conditions, the interaction thickness is *c.* $450\ \text{nm}$. Slabs of the porphyroclastic peridotites were cut based on their CPO in order to have, for the majority of the crystals composing the rock, two of the main olivine crystallographic axes: [100] and [010] or [100] and [001] in the plane of the section. The orientation of the analyzed crystals was checked by EBSD.

Observations

Coarse olivine crystals in the porphyroclastic peridotites display low dislocation densities ranging from 0.5×10^{11} to $4 \times 10^{11}\ \text{m}^{-2}$ (Table 1). This allows easy observation of the dislocation structures both in transmitted light (Fig. 14) and by electron back-scattered imaging (Fig. 15). Some rare crystals yield much higher dislocation densities that cannot be characterized by optical observation. A large variety of dislocation structures is observed. In crystals cut parallel to (010), the most pre-eminent features are straight dislocation walls normal to [100] that crosscut the whole crystal (black arrows in Fig. 14a, b and e). They represent subgrain boundaries that are spaced at $10\text{--}55\ \mu\text{m}$. Free dislocations with lines roughly parallel to [100] branch from these (100) subgrain boundaries (Fig. 14a, b and e). These dislocations are classically interpreted as screw dislocations with a [100] Burgers vector (Nicolas & Poirier, 1976). However, some of these dislocation lines have festoon shapes (white arrow in Fig. 14b) suggesting pinning by defects while moving in the [001] direction; they might represent edge dislocations with a [001] Burgers vector. A second family of dislocation walls, which is in a plane oblique to the thin-section plane but containing [100] (i.e. parallel to a $\{0kl\}$ plane) is also locally observed (white arrows in Fig. 14a). Finally, the presence of open dislocation loops (Fig. 14b) suggests activation of cross-slip.

Olivine crystals in the fine-grained equigranular peridotite AV16 are almost devoid of dislocations (Fig. 14c). Rare dislocations are observed around inclusions. Extremely low dislocation densities also characterize small olivine crystals ($<500\ \mu\text{m}$) within a 5 mm wide vein filled by the fine-grained ol-opx-oxides \pm amph \pm cpx \pm glass matrix that crosscuts the porphyroclastic peridotite AV1 (Fig. 14d and f). In contrast, the dislocation densities and structures of coarse olivine crystals outside the vein are similar to those in other porphyroclastic peridotites (Fig. 14e). A steep transition between the two dislocation structures takes place at the vein wall. However, the dislocation

Sample	Correlation between ol & opx CPO	Relative concentration of olivine [010] & [001] axes	Rotation axes	Sample	Correlation between ol & opx CPO	Relative concentration of olivine [010] & [001] axes	Rotation axes
AV1	Not enough Opx measured in thin section	1.29	 MD = 9.92 N = 5941	AV14	[001]opx not // [100]ol	1.89	 MD = 12.18 N = 5886
AV2	[001]opx not // [100]ol	0.99	 MD = 13.66 N = 11084	AV15	[001]opx not // [100]ol	1.25	 MD = 12.07 N = 10208
AV3	[100]ol // [001]opx [001]ol // [100]opx	1.49	 MD = 15.52 N = 1933	AV16	[001]opx not // [100]ol	1.21	 MD = 1.86 N = 4635
AV4	[100]ol // [001]opx [010]ol // [100]opx	1.10	 MD = 8.26 N = 3642	AV18	[100]ol // [001]opx [010]ol // [100]opx	0.74	 MD = 10.81 N = 11533
AV5	Not enough Opx measured in thin section	1.57	 MD = 8.19 N = 4219	AV19	[001]opx not // [100]ol	1.73	 MD = 11.33 N = 11051
AV6	Not enough Opx measured in thin section	1.06	 MD = 9.79 N = 4853	AV20	[001]opx not // [100]ol	1.22	 MD = 9.30 N = 11063
AV7	[100]ol // [001]opx [010]ol // [100]opx	1.04	 MD = 9.70 N = 21201	AV21	[001]opx not // [100]ol	1.19	 MD = 10.56 N = 4462
AV8	[001]opx not // [100]ol	1.50	 MD = 8.31 N = 7664	AV23	[100]ol // [001]opx [010]ol // [100]opx	0.83	 MD = 7.34 N = 6707
AV9	[001]opx not // [100]ol	1.01	 MD = 10.50 N = 9190	AV25	[001]opx not // [100]ol	1.09	 MD = 11.26 N = 12286
AV10	[001]opx not // [100]ol	0.89	 MD = 9.82 N = 12535	AV27	[100]ol // [001]opx [001]ol // [100]opx	1.02	 MD = 9.87 N = 11156
AV11	[001]opx not // [100]ol	0.86	 MD = 8.29 N = 3689				
AV12	[100]ol // [001]opx [001]ol // [100]opx	1.04	 MD = 14.43 N = 16296				
AV13	[100]ol // [001]opx [010]ol // [100]opx	1.32	 MD = 10.40 N = 5944				



MD = Maximum of density in MUD*
 Contours at 2 MUD* intervals
 N = Number of measurements
 *MUD = Multiple of Uniform Distribution

Fig. 13. Comparison of various parameters used for identifying the dominant slip plane in olivine: (1) correlation between olivine and orthopyroxene CPO, (2) relative concentrations of olivine [010] and [001] axes, and (3) rotation axes accommodating misorientations $\leq 10^\circ$ within olivine crystals. Samples highlighted in grey have correlated olivine and orthopyroxene CPO; that is, the angle between the maximum concentration of [100] olivine axes and [001] orthopyroxene is $< 20^\circ$. For these samples, the comparison between orthopyroxene and olivine CPO may be used to identify the dominant slip plane in olivine. Relative concentrations of olivine [010] and [001] axes are quantified by the ratio of the density maxima of the [010] and [001] axes. Rotation axes are represented as inverse pole figures in the crystal reference frame; for sample AV16 they are represented as points instead of as density contours at two multiples of a uniform distribution because they are almost random.

Table 1: Deviatoric stresses estimated from free dislocation density

Sample	Number of analyzed grains	Dislocation density ($\times 10^{11} \text{ m}^{-2}$)	Standard deviation ($\times 10^{11} \text{ m}^{-2}$)	Average stress (MPa)	Minimum stress (MPa)	Maximum stress (MPa)
AV1	4	3.37	0.45	58.05	54.04	61.81
AV3	4	1.67	0.91	40.87	27.57	50.79
AV23	3	2.06	0.99	45.39	32.71	55.23

density in the coarse olivine crystals in contact with the vein tends to be lower than that in grains several millimeters away from it (Fig. 14g). The observed decrease in the dislocation density suggests that diffusional processes were enhanced within and around these veins.

FTIR ANALYSES OF WATER CONTENTS IN OLIVINES AND ORTHOPYROXENES

Analytical procedure

Unpolarized Fourier Transform infra-red (FTIR) spectroscopy measurements were performed using a Bruker Vertex70 spectrometer coupled with a Bruker Hyperion microscope at the Laboratoire Magmas et Volcans (LMV) in Clermont-Ferrand (France) and using a Bruker IFS66v coupled with a Bruker IR microscope at the Laboratoire des Colloïdes, Verres et Nanomatériaux (LCVN) in Montpellier (France). Both microscopes were equipped with all-reflecting Cassegrainian optics, a condenser, and a 15 \times objective. Analyses were made at room pressure and temperature. Mid-IR measurements were performed using a Globar light source, a KBr beam splitter, a high-sensitivity DTGS (deuterated triglycine sulfate) at the LMV and a high-sensitivity MCT (DTGS) at the LCVN, both cooled by liquid nitrogen. Spectra were acquired with a resolution of 4 cm^{-1} and at least 100 scans were accumulated for each spectrum (Table 2). As these were open-air analyses, a background correction had to be performed on each measurement to remove the contribution of the vapour phase. This was done by always performing two analyses, one without and another with the sample; the difference between the two yields the spectrum used for the determination of the water contents in the minerals. This background correction and the baseline correction were carried out using the OPUS software.

Unpolarized FTIR absorption spectra of olivines and orthopyroxenes were obtained on doubly polished sections with a thickness of $\sim 500 \mu\text{m}$. Thinner sections, 250–150 μm thick, were used for measuring water contents in

fine-grained olivines in the equigranular peridotite AV16 and in the coarse porphyroclastic samples AV10 and AV15 (Table 2). The detection limit at the lowest sample thickness is 1 ppm. The sections were left in an acetone bath for at least 12 h to remove any residual glue. Measurements were performed in selected crack- and inclusion-free grains (optical observation) using a square or circular aperture at LMV and LCVN, respectively, with a diameter between 90 and 105 μm as a function of the analyzed grain size (Table 2). Measurements in orthopyroxenes were hindered by the large amount of inclusions in the coarse crystals and by the fine-grained texture of the acicular aggregates. Most measurements were performed at the grains' core, which should be least affected by late, extraction-related water loss (Demouchy *et al.*, 2006).

The water concentration in the analyzed minerals was calculated by integrating the absorption bands according to the calibration of Paterson (1982):

$$C_{\text{OH}} = \frac{X_i}{150\zeta} \int \frac{K(\bar{\nu})}{(3780 - \bar{\nu})} d\bar{\nu} \quad (1)$$

where C_{OH} is the hydroxyl concentration (in $\text{H}/10^6 \text{ Si}$ or ppm wt H_2O), ζ is an orientation factor (1/3 for unpolarized measurements), and $K(\bar{\nu})$ is the absorption coefficient in cm^{-1} for a given wavenumber $\bar{\nu}$. X_i is a density factor; its value for olivine and orthopyroxene is 2695 and 2769 wt ppm H_2O , respectively [see Bolfan-Casanova *et al.* (2000) for calculation method]. The calibration of Paterson (1982) underestimates the water concentration in olivine compared with the calibration proposed by Bell *et al.* (2003). However, the Bell *et al.* (2003) calibration may be applied only to olivine spectra dominated by high wavenumber (3650–3450 cm^{-1}) OH absorption bands. This is not the case for olivine in the studied Avacha peridotites, whose spectra are dominated by low wavenumber absorption bands (Fig. 16). Moreover, the calibration of Paterson (1982) has the advantage of allowing direct comparison of water contents in olivine and pyroxenes (Bolfan-Casanova *et al.*, 2000). Errors on the absolute water contents are, however, of $\pm 30\%$ (Kohlstedt *et al.*, 1996).

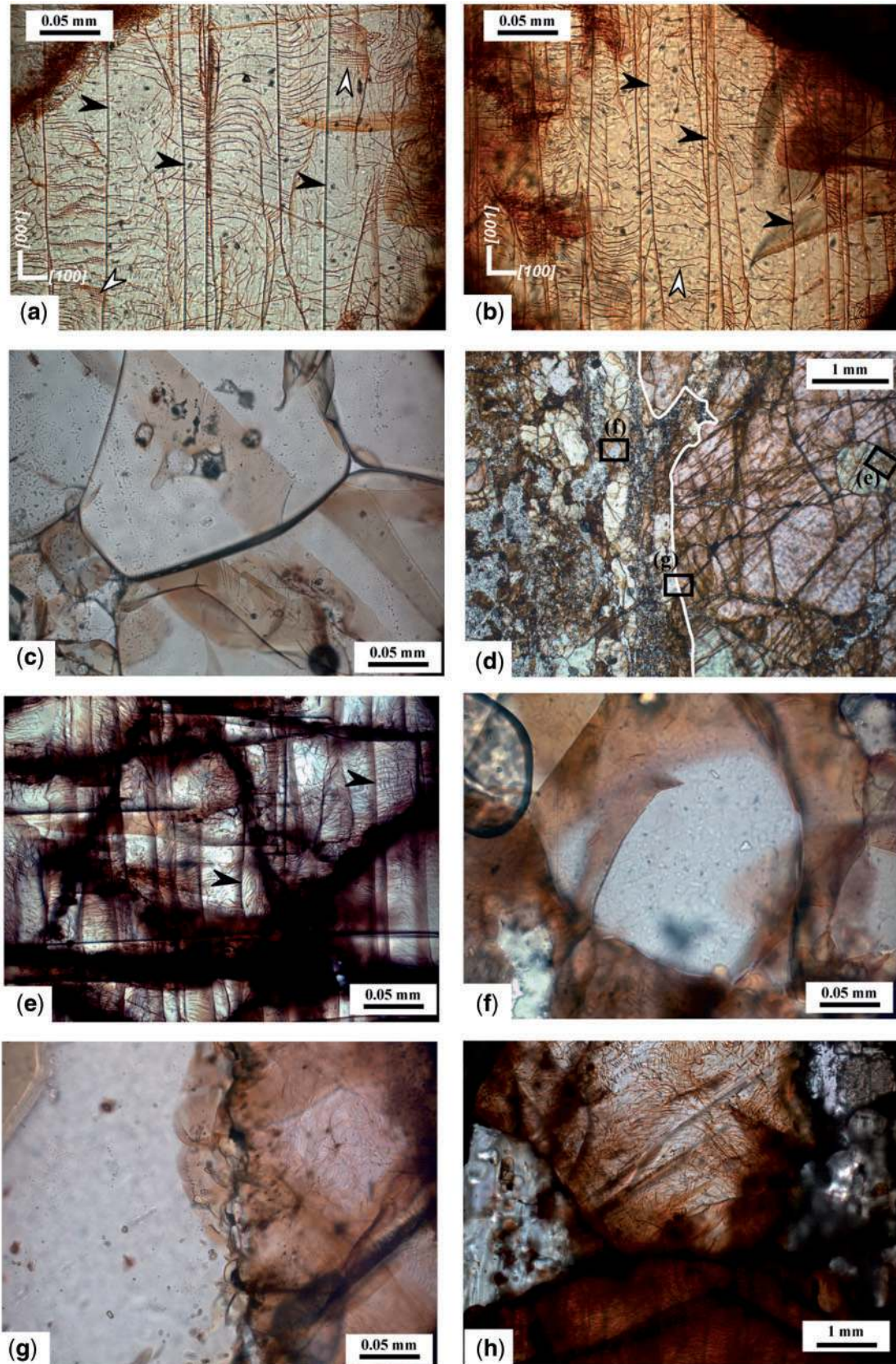


Fig. 14. Photomicrographs (plane-polarized light) of decorated dislocations in olivine. (a, b) Dislocation structures seen on two olivine crystal cut on planes close to (010); black arrows indicate the dominant (100) subgrain boundaries. In (a) the white arrow marks a subgrain boundary oblique to the section plane, which is formed by dislocations of two slip systems with perpendicular Burgers vectors, probably [100] and [001]. In (b) the white arrow shows festoon-like dislocation lines that may represent pinned edge dislocations with [001] Burgers vectors. (c) Small olivine crystals totally free of dislocations and displaying an open triple junction in fine-grained peridotite AV16. (d) Lower enhancement image of sample AV1 showing the change in dislocation structure and density between olivine crystals that form a coarse porphyroclastic microstructure and small polygonal olivine crystals in a vein filled by the fine-grained matrix; the white line marks the edge of the vein. Black rectangles show the location of photomicrographs (e–g). (h) Variations in dislocation densities between neighbouring olivine crystals with different orientations in coarse porphyroclastic peridotite AV20.

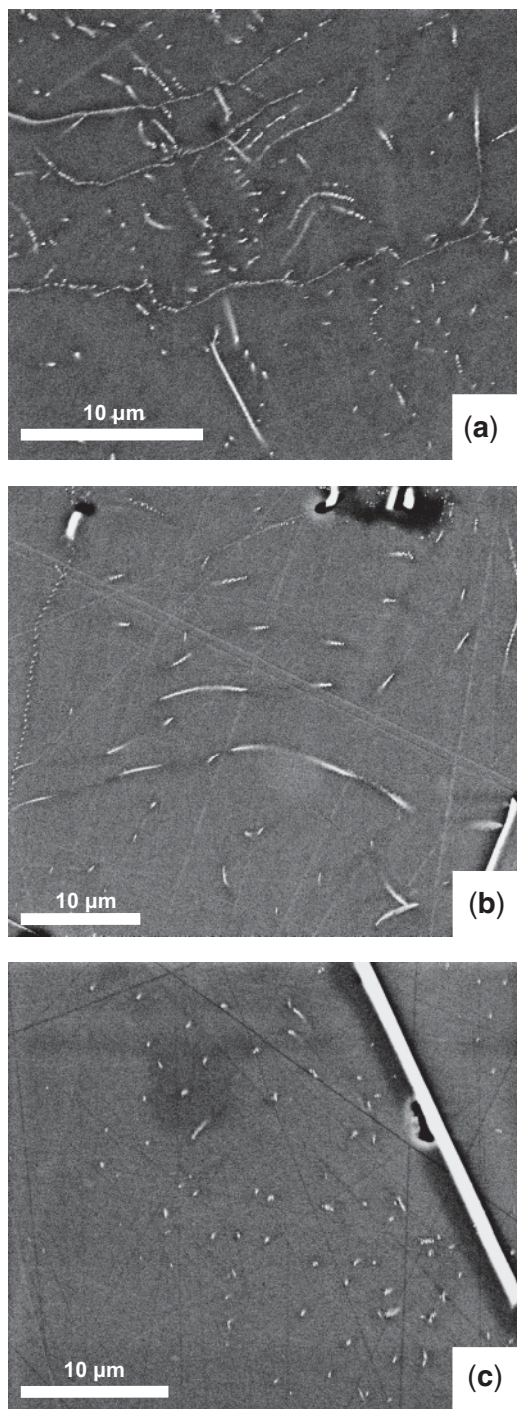


Fig. 15. Backscattered electron (BSE) image of dislocations (white lines or points as a function of the angle between the dislocation line and the observation surface) in olivine crystals from coarse porphyroclastic peridotites AV1 (a), AV23 (b), and AV3 (c). Densities estimated using the intercept length method are 3.86×10^{11} , 1.92×10^{11} , and $0.55 \times 10^{11} \text{ m}^{-2}$, respectively.

Results: IR spectra and water solubility

Figure 16 shows typical unpolarized FTIR spectra for olivines and orthopyroxenes in xenoliths AV1, AV3, AV10, AV15, AV16 and AV23. The olivine spectra are rather homogeneous. The major O–H absorption bands are at 3354 and 3328 cm^{-1} . In contrast, the band at 3574 cm^{-1} , where the maximum O–H absorbance is often observed in natural peridotites (Miller *et al.*, 1987; Bell *et al.*, 2004; Demouchy, 2004; Demouchy *et al.*, 2006; Peslier & Luhr, 2006; Grant *et al.*, 2007), displays only a minor peak. The observed spectra are nevertheless similar to those of olivines in peridotite xenoliths from Mexico, Kenya, and the Carpathians (Miller *et al.*, 1987; Falus *et al.*, 2008) and of olivine ($\text{Mg}_{1.8}\text{Fe}_{0.2}\text{SiO}_4$) in equilibrium with orthopyroxene in the experimental sample of Berry *et al.* (2005). Water contents in the studied samples range from 1 to $8.3 \text{ ppm H}_2\text{O}$ by weight (Table 2). The water content varies as a function of the grain size: coarse ($>1 \text{ mm}$), intermediate ($0.5\text{--}1 \text{ mm}$) and fine ($<0.5 \text{ mm}$) olivine crystals show on average 6.1 , 3.4 and $2.4 \text{ ppm H}_2\text{O}$, respectively (Table 2). These values are in the same range as the water contents in olivine from spinel-peridotite xenoliths sampling the continental lithosphere above the western North America, Patagonia and Carpathian subduction zones (Demouchy, 2004; Peslier & Luhr, 2006; Falus *et al.*, 2008).

Orthopyroxene spectra are characterized by major O–H absorption bands at 3596 , 3543 , and 3520 cm^{-1} and by broader minor peaks around 3420 , 3317 and 3070 cm^{-1} (Fig. 16b). This pattern is typical for orthopyroxene from mantle xenoliths (Peslier *et al.*, 2002; Grant *et al.*, 2007). Water contents are however very heterogeneous, varying from 25 to 506 ppm (Table 2). Although there is a clear variation in water contents from sample to sample, strong heterogeneity is also observed within samples (Table 2). Orthopyroxenes in coarse-grained porphyroclastic peridotite AV15 and in equigranular peridotite AV16 have abnormally low water contents ($25\text{--}128 \text{ ppm}$) for subduction zone xenoliths (Peslier & Luhr, 2006; Falus *et al.*, 2008). AV10 has the most water-rich orthopyroxenes ($218\text{--}506 \text{ ppm}$). The latter value ($>500 \text{ ppm H}_2\text{O}$) represents an abnormally high water content for spinel peridotites; however, the spectra of the two orthopyroxenes are consistent and do not show evidence for contamination of the measurements by water-rich inclusions or amphibole lamellae (typical peak at 3900 cm^{-1}).

There is a weak positive correlation between the average water contents in olivine and orthopyroxene in each sample. Concentration ratios (R_c) calculated using the mean water contents in olivine and orthopyroxene in each sample are 18.6 in AV15, 20.9 in AV16, 39.5 in AV3, and 76 (Table 2) in AV10. These concentration ratios, although extremely variable, are within the range of published values of water partitioning coefficients between olivine

Table 2: Water contents in olivines and orthopyroxenes

Sample	Mineral	Laboratory	Number of accumulated scans	Aperture size (mm)	Section thickness (cm)	Water content* (wt ppm H ₂ O)	Water content* (H/10 ⁶ Si)	Grain size (mm)	Peridotite type
AV1	ol-1	LMV	300	0.1	0.0552	5.1	78.438	>1	CG
AV1	ol-2	LMV	300	0.1	0.0552	8	123.04	>1	CG
AV3	ol-1	LMV	300	0.1	0.0580	2.3	35.374	0.5–1	CG
AV3	ol-2	LMV	300	0.1	0.0580	7.2	110.736	>1	CG
AV3	opx-1	LMV	300	0.1	0.0580	188	2891.44	—	CG
AV10	ol-1	LCVN	300	0.09	0.0252	7	107.66	>1	CG
AV10	ol-2	LCVN	300	0.09	0.0252	4	61.52	0.5–1	CG
AV10	ol-3	LCVN	300	0.09	0.0252	4	61.52	0.5–1	CG
AV10	ol-4	LCVN	300	0.09	0.0264	4	61.52	<0.5	CG
AV10	opx-1	LCVN	300	0.075	0.0252	218	3352.84	—	CG
AV10	opx-2	LCVN	300	0.09	0.0300	506	7782.28	—	CG
AV15	ol-1	LCVN	300	0.09	0.0184	4	61.52	>1	CG
AV15	ol-2	LCVN	300	0.09	0.0184	3	46.14	<0.5	CG
AV15	ol-3	LCVN	300	0.09	0.0184	3	46.14	<0.5	CG
AV15	ol-4	LCVN	300	0.09	0.0184	2	30.76	<0.5	CG
AV15	ol-5	LCVN	300	0.09	0.0184	2	30.76	<0.5	CG
AV15	ol-6	LCVN	300	0.09	0.0184	2	30.76	<0.5	CG
AV15	ol-7	LCVN	300	0.09	0.0184	4	61.52	>1	CG
AV15	ol-8	LCVN	300	0.09	0.0184	3	46.14	<0.5	CG
AV15	ol-9	LCVN	300	0.09	0.0184	3	46.14	<0.5	CG
AV15	ol-10	LCVN	300	0.09	0.0184	5	76.9	>1	CG
AV15	ol-11	LCVN	300	0.09	0.0184	5	76.9	>1	CG
AV15	opx-1	LCVN	300	0.09	0.0184	55	845.9	—	CG
AV15	opx-2	LCVN	300	0.09	0.0184	128	1968.64	—	CG
AV15	opx-3	LCVN	300	0.09	0.0184	35	538.3	—	CG
AV15	opx-4	LCVN	300	0.09	0.0184	25	384.5	—	CG
AV16	ol-1	LCVN	100	0.09	0.0163	3	46.14	<0.5	FG
AV16	ol-2	LCVN	100	0.09	0.0163	2	30.76	<0.5	FG
AV16	ol-3	LCVN	100	0.09	0.0163	3	46.14	<0.5	FG
AV16	ol-4	LCVN	200	0.105	0.0163	1	15.38	<0.5	FG
AV16	opx-1	LCVN	200	0.105	0.0163	47	722.86	—	FG
AV23	ol-1	LMV	300	0.1	0.0552	6.6	101.508	>1	CG
AV23	ol-2	LMV	300	0.1	0.0552	7.3	112.274	>1	CG
AV23	ol-3	LMV	300	0.1	0.0552	8.3	127.654	>1	CG

CG, coarse-grained peridotite; FG, fine-grained peridotite. LMV, Laboratoire Magmas et Volcans, Université Clermont-Ferrand, France. LCVN, Laboratoire des Colloïdes, Verres et Nanomatériaux, Université Montpellier 2, France. *Calibration of Paterson (1982). Water contents have $\pm 30\%$ error.

and orthopyroxene ($D_{\text{water}}^{\text{opx/ol}}$) in spinel-lherzolites: 40.7 ± 19.8 (Grant *et al.*, 2007). Because the water contents in olivine vary as a function of grain size and because water contents in the orthopyroxenes are extremely heterogeneous, the R_c values calculated using single olivine–orthopyroxene pairs show an even greater dispersion,

varying from five in AV15 (ol10–opx4) to 126.5 in AV10 (ol2–opx2). These extreme concentration ratios are not pertinent to equilibrium water partitioning between mantle minerals, but rather reflect the heterogeneity of water distribution in orthopyroxene and compositional disequilibrium in the studied samples.

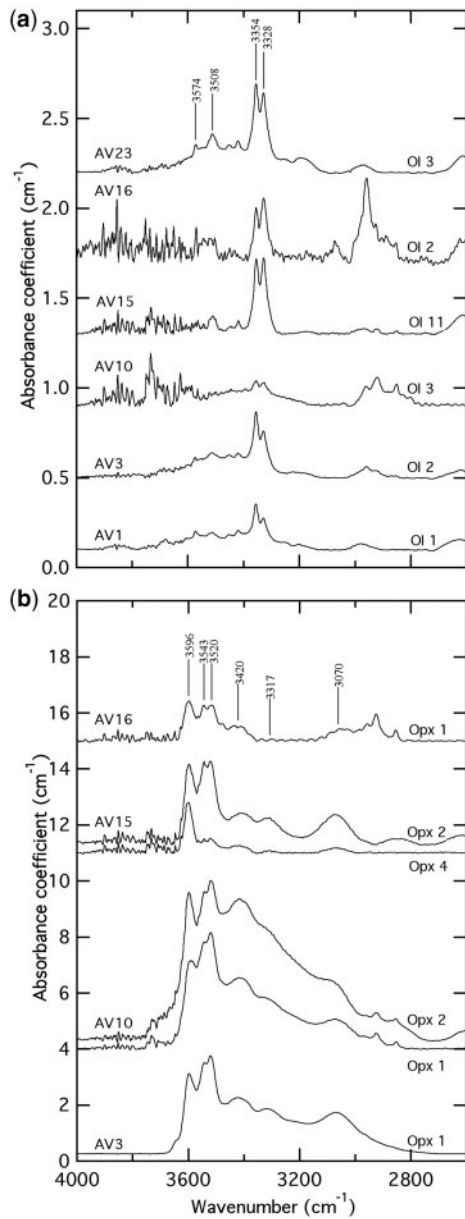


Fig. 16. Unpolarized IR spectra for the most representative olivine (a) and orthopyroxene (b) of each sample. As the water content in orthopyroxenes is highly heterogeneous, even within a single sample, we plotted the two spectra corresponding to the two extreme values measured for each sample (Table 3). Spectra are normalized to 1 cm^{-1} .

DEVIATORIC STRESS ESTIMATES

In deformation by dislocation creep, the density of dislocations (ρ) in a crystal depends on the applied stress (Poirier, 1985):

$$\rho = \alpha b^{-2} (\sigma/\mu)^2 \quad (2)$$

where α is a non-dimensional constant of order unity, b is the Burgers vector, σ is the stress and μ the shear modulus.

Analysis of the microstructure of experimentally deformed olivine-rich rocks highlights that the applied differential stress is proportional to the free dislocations density (e.g. Kohlstedt & Goetze, 1974), to the average subgrain size (e.g. Raleigh & Kirby, 1970; Karato *et al.*, 1980), or to the average recrystallized grain size (e.g. Mercier *et al.*, 1977; Karato *et al.*, 1980; Van der Wal *et al.*, 1993). However, these microstructural parameters have different stabilities relatively to annealing or changes in stress. Free dislocation densities are easily reduced by post-kinematic annealing. They also readily re-equilibrate in response to changes in the stress field, in particular to a stress increase, even if the associated strain is very small. Subgrain and recrystallized grain sizes are more stable features that need long annealing times (or high temperatures) or significant finite strains to be modified. In the following discussion, we compare the stresses estimated using these three paleopiezometers for the Avacha peridotites.

Free dislocations density

To estimate the free dislocations density we used the method described by Hirsch *et al.* (1965), which consists of measuring the total dislocation lines length in a unit volume of the crystal. The total dislocation lines length in a crystal was estimated by the intersection analysis method (Ham, 1961) applied to the BSE images (Fig. 15). The density of dislocations Λ is defined as

$$\Lambda = 2N/Lt \quad (3)$$

where N is the number of intersections, L is the total length of lines composing the random network, and t is the thickness of the observation zone ($\approx 450 \text{ nm}$, which is the BSE interaction depth in the present case).

During plastic deformation, crystals are submitted to variable stresses according to their orientation and to heterogeneity in the deformation between neighbouring grains. These stress gradients may be high for low-symmetry minerals such as olivine that show a high plastic anisotropy (Bai *et al.*, 1991), leading to highly variable dislocation densities within a rock sample. Such variable dislocation densities are observed in the decorated sections of the coarse-grained Kamchatka peridotites (Fig. 14h). In the present study, we selected optically three or four representative olivine crystals (i.e. displaying an 'average' dislocation density) in coarse-grained porphyroclastic peridotites AV1, AV3 and AV23. Dislocation densities estimated using both optical and SEM observations in these crystals range from 0.5×10^{11} to $4 \times 10^{11} \text{ m}^{-2}$ (Table 1). Based on the stress vs dislocation density relation given by Kohlstedt *et al.* (1976a), these observed dislocation densities record deviatoric stresses ranging from 28 to 62 MPa.

As discussed above, a major inconvenience of this paleopiezometer is that the free dislocations density is not

stable against variations in stress or annealing (Poirier, 1985). The preservation of highly variable dislocation densities within a sample suggests limited annealing. One cannot exclude, however, an effect of a weak, low-temperature, high-stress deformation in the lithosphere or during extraction on the observed free dislocation density.

Subgrain size

Karato *et al.* (1980) obtained the following relationship between stress and the subgrain boundary spacing in olivine single crystals deformed under high-temperature conditions:

$$d_s = 280\sigma^{-0.67} \quad (4)$$

where d_s is the subgrain boundary spacing in μm and σ is the stress in MPa. The spacing between adjacent (100) subgrain boundaries measured in 25 olivines from four decorated coarse porphyroclastic peridotites varies between 10 and 150 μm (Fig. 14a and b), with an average at 32.5 μm (the median is at 30 μm). The mean values correspond to paleo-stresses of 43.5 MPa, and extreme values range from 130 to 2.5 MPa, respectively.

The average subgrain size should vary rapidly with increasing stress, but remain stable under decreasing stress conditions. This paleopiezometer should therefore be representative of the maximum stress experienced by a crystal (Poirier, 1985). As discussed above, during deformation, crystals are submitted to variable stresses according to their orientation and to the heterogeneity of deformation between neighbouring grains. This may partially explain the high variability in subgrain boundary spacing recorded in our samples. However, 50% of the measured subgrains are spaced by 20 to 40 μm . This implies that the mean value of the stress (43.5 MPa) obtained by this method could be representative of the maximum stress to which the studied samples were exposed.

Recrystallized grain size

All empirical relations between recrystallized grain sizes and deviatoric stresses follow a power law:

$$D_g = A\sigma^{-n} \quad (5)$$

where D_g is the recrystallized grain size, σ is the differential stress, and A and n are empirical constants obtained by fitting experimental data. In this study, we used (1) the calibration of Karato *et al.* (1980), which is based on single crystal deformation experiments, (2) the calibrations of Van der Wal *et al.* (1993), and (3) those of Zhang *et al.* (2000), which are derived from deformation experiments on olivine-rich polycrystals, and the calibration of Jung & Karato (2001b) derived from deformation experiments on hydrated olivine (Table 3).

Table 3: Parameters for equation (5)

Paleopiezometer	A	n
Karato <i>et al.</i> (1980)	8300	1.18
Van der Wal <i>et al.</i> (1993)	15000	1.33
Zhang <i>et al.</i> (2000)*	3544	1.23
Jung & Karato (2001b)*	67103	1.45

*Calculated by regression through their data.

Grain sizes in the coarse-grained porphyroclastic peridotites were estimated from the EBSD maps. Measured mean intercept lengths were multiplied by a geometric factor of 1.2 to convert the grain size in thin section to a three-dimensional grain diameter (Van der Wal *et al.*, 1993). An inconvenient aspect of this technique is that the minimum observed grain size is limited by the EBSD measurement step size. This leads to some bias in the estimation of the smaller grain sizes, even if all maps were obtained with measurement steps at least four times smaller than the initial (optical) estimation of the average grain size.

In coarse-grained porphyroclastic peridotites, such as the studied Kamchatka xenoliths, that show a continuous grain size distribution (Fig. 17), the main difficulty, however, is to discriminate between porphyroclasts and recrystallized grains. For all coarse-grained porphyroclastic xenoliths, more than 75% of the measured olivine grains are smaller than 750 μm , whereas 75% of the thin-section area is occupied by grains larger than 750 μm . We cannot discriminate the porphyroclasts from the recrystallized grains, but we assume that the majority of the latter have a grain size lower than 750 μm and choose to use the mean grain size in a sample as the recrystallized grain size. Average grain sizes range from 300 to 800 μm (Table 4). In this grain size range, the Van der Wal *et al.* (1993) and Zhang *et al.* (2000) calibrations give the maximum and minimum stress estimates for dry conditions, respectively (Table 4, Fig. 18). Recrystallized grain sizes of 307–797 μm correspond to stresses of 9–18 MPa or 3–11 MPa. Higher stresses (21–41 MPa) are estimated for deformation under hydrated conditions, consistent with data suggesting faster grain growth under hydrated conditions. However, this latter estimation should be used with caution, because water contents in the Kamchatka olivines (Table 2) are much lower than those in the Jung & Karato (2001b) samples (50 wt ppm or 800 H/10⁶ Si).

The recrystallized grain size is the most stable paleopiezometer and could reflect the last high-temperature deformation episode. However, uncertainty in the determination of the equilibrium recrystallized grains size hinders its use. Moreover, in the studied Kamchatka xenoliths,

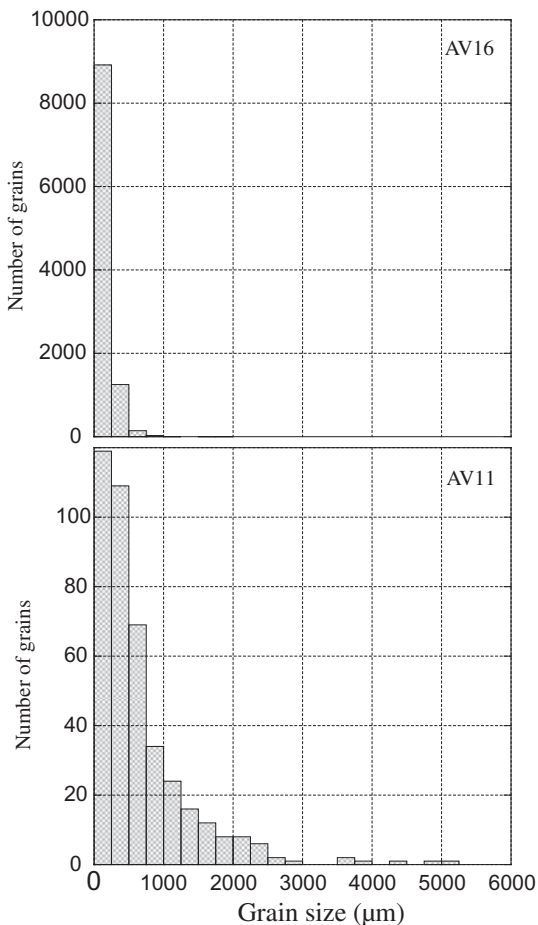


Fig. 17. Olivine grain size histograms for samples AV16 and AV11.

olivine grain sizes were also modified by reaction with percolating fluids that led to crystallization of orthopyroxene at the expense of olivine (Figs 3 and 4a) and, in the opx-rich bands, olivine grain growth may have been limited by interstitial orthopyroxene. Grain sizes in these bands are thus probably minimum values, leading to overestimation of stresses in the opx-rich samples.

DISCUSSION

Thermo-mechanical history of the Avacha spinel-harzburgites

Peridotite xenoliths from the Avacha volcano are highly refractory spinel harzburgites. Primary cpx is absent, and secondary cpx (≤ 3 vol. %) occurs only as interstitial crystals in the fine-grained matrix (Ionov, 2010). Modal and whole-rock chemical compositions suggest therefore that these xenoliths are the residues of high-degree (30–40%) partial melting at shallow depths (< 1 to 2 GPa, Ionov, 2009). On the other hand, widespread unmixing and core–rim compositional gradients in coarse orthopyroxene

crystals record slow cooling to temperatures $< 900^\circ\text{C}$ (Ionov, 2010), indicating that these peridotites were part of the lithospheric mantle at the time of their extraction by the host andesitic magmas. The analysis of microstructures and crystal preferred orientations in the xenoliths implies that they underwent a complex history involving deformation and fluid and/or melt percolation at variable temperature conditions. Unravelling the chronology of the thermal, chemical and deformation events recorded by these peridotites is essential to determine if these events are related to the subduction process.

Except for one sample, the Avacha xenoliths exhibit coarse-grained porphyroclastic microstructures characterized by a lineation marked by coarse elongated olivine crystals with sinuous grain boundaries, widely spaced sub-grain boundaries, low free dislocation densities, and well-developed olivine CPO. These microstructures are characteristic of deformation by dislocation creep under high-temperature, low deviatoric stress conditions, where dislocation glide is assisted by diffusional processes, such as climb and grain boundary migration. These deformation conditions are consistent with the measured olivine CPO that implies dominant activation of the high temperature, low-pressure $\{0kl\}[100]$ slip systems with dominant activation of the (010) and (001) planes. The activation of multiple $\{0kl\}$ slip planes may have been favoured by decreasing temperature conditions (Durham *et al.*, 1977) or by deformation under moderately hydrous conditions (Mackwell *et al.*, 1985; Katayama *et al.*, 2004). Hydrous conditions also enhance diffusion rates, lowering the viscosity of mantle rocks (Blacic, 1972; Mei & Kohlstedt, 2000a) and favouring recrystallization and grain growth (Karato, 1989; Jung & Karato, 2001b) and, hence, development of coarse-grained, well-recovered microstructures, like those observed in the studied xenoliths, at lower temperatures. Taken together, the microstructural observations and the CPO suggest that the major deformation episode recorded by these xenoliths took place under low-stress conditions like those that probably prevail in the asthenosphere or at the base of the lithosphere. Later deformation under higher stress, lower temperature conditions is consistent with the higher deviatoric stresses (28–62 MPa) estimated from dislocation densities. A cooling history is also consistent with the brittle character (veins) of the late fluid transport structures (Fig. 4e and f) in the Kamchatka xenoliths.

Comparison of the paleo-stresses estimated from free dislocation densities and recrystallized grain sizes with rheological profiles (Fig. 19) calculated using a geothermal gradient for a mature volcanic arc, such as Kamchatka, and empirical flow laws for dry and wet dunite (Chopra & Paterson, 1981, 1984) allow discussion of the rheological behaviour and strain rates and location in the supra-subduction mantle. For a regional surface heat flow

Table 4: Deviatoric stresses estimated from recrystallized grain sizes

Sample	Recrystallized grain size (μm)	Corrected (3D) recrystallized grain size (μm)	Stress (MPa)			
			Karato <i>et al.</i> (1980)	Van der Wal <i>et al.</i> (1993)	Zhang <i>et al.</i> (2000)	Jung & Karato (2001)
AV1	476.0	571.2	9.7	11.7	4.4	26.9
AV2	362.0	434.4	12.2	14.3	5.5	32.5
AV3	583.6	700.3	8.1	10.0	3.7	23.4
AV4	512.0	614.4	9.1	11.0	4.2	25.6
AV5	307.8	369.3	14.0	16.2	6.3	36.4
AV6	632.1	758.6	7.6	9.4	3.5	22.1
AV7	501.2	601.4	9.2	11.2	4.2	26.0
AV8	424.9	509.9	10.6	12.7	4.9	29.1
AV9	462.3	554.8	9.9	11.9	4.5	27.5
AV10	352.3	422.7	12.5	14.6	5.7	33.2
AV11	664.8	797.8	7.3	9.1	3.4	21.4
AV12	500.7	600.8	9.3	11.2	4.2	26.0
AV13	558.4	670.0	8.4	10.4	3.9	24.1
AV14	412.6	495.1	10.9	13.0	5.0	29.7
AV15	395.8	474.9	11.3	13.4	5.1	30.6
AV16	157.5	189.0	24.7	26.8	10.9	57.8
AV18	443.5	532.2	10.3	12.3	4.7	28.3
AV19	255.9	307.1	16.3	18.6	7.3	41.4
AV20	349.4	419.3	12.6	14.7	5.7	33.4
AV21	482.6	579.1	9.5	11.6	4.4	26.7
AV23	617.1	740.5	7.8	9.6	3.6	22.5
AV25	348.0	417.6	12.6	14.8	5.7	33.4
AV27	409.1	491.0	11.0	13.1	5.0	29.9

of 88 mW/m^2 (Currie & Hyndman, 2006), the base of the lithosphere, which we assume to be defined by the 1200°C isotherm, is located at $c. 70 \text{ km}$. Furthermore, temperatures of 900°C , which correspond to the maximum estimates from two-pyroxene thermometry, are reached at $c. 45 \text{ km}$ depth.

For strain rates of 10^{-14} s^{-1} (10^{-15} s^{-1}) and a dry peridotite flow law, stresses equivalent to those estimated from the free dislocation density and recrystallized grain size are obtained for depth of 47–42 km (38–43 km) and 50–64 km (45–58 km), respectively. The last stages of deformation, which control in particular the free dislocation density, may thus have occurred in the upper part of the lithospheric mantle, from where the xenoliths were extracted. However, the recrystallized grain sizes record instead a deformation in the lower lithosphere, below 45–50 km. However, the reaction forming orthopyroxene at the expense of olivine may have modified the olivine

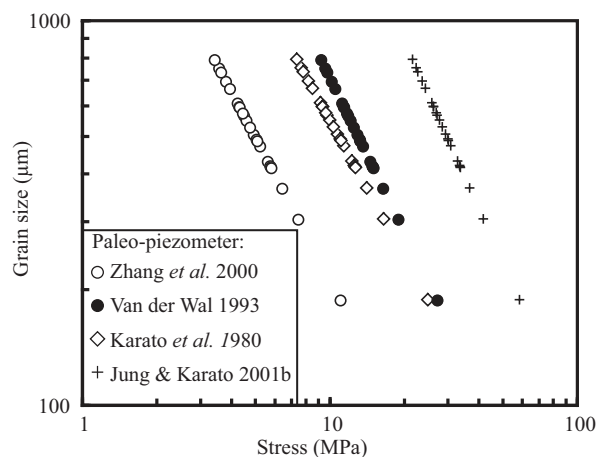


Fig. 18. Deviatoric stresses estimated using different paleo-piezometers vs average olivine recrystallized grain size for all studied samples.

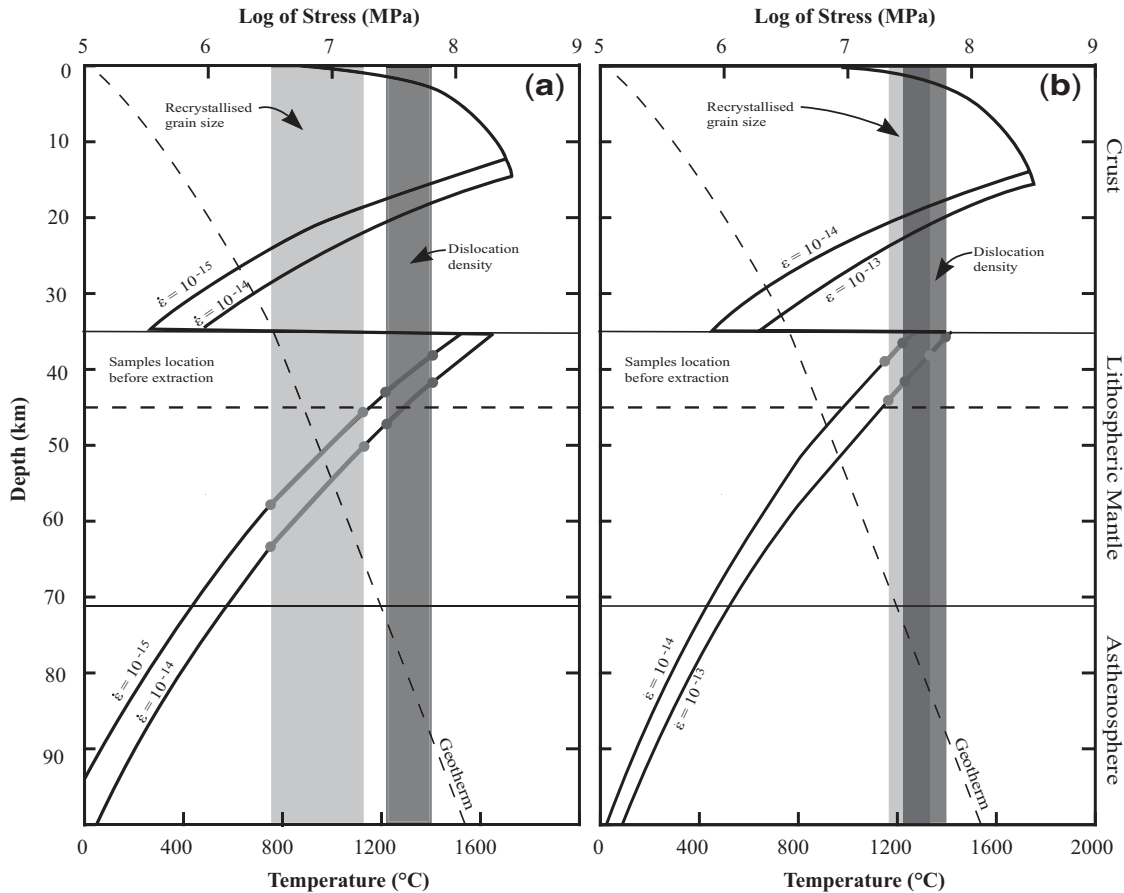


Fig. 19. Rheological profiles of the lithosphere beneath the Kamchatka active volcanic arc considering a dry (a) or a wet (b) mantle. We assumed a granodioritic crust with a thickness of 35 km (Zhuravlev & Antipov, 1993; Kharakhin, 1996), a surface heat flow of 88 mW/m² (Currie & Hyndman, 2006), and a constant thermal conductivity of 2.51 and 3.35 W/m K for the granodiorite and peridotite layers, respectively (Philpotts, 1990). The brittle upper crust strength was estimated using Byerlee (1978) and the lower crust strength by using a dry granodiorite power law (Ranalli, 1995). The mantle strength was calculated using either the dry or the wet dunite flow laws of Chopra & Paterson (1981, 1984). $\dot{\epsilon}$ is the strain rate given in s⁻¹. Light and dark grey bands indicate deviatoric stresses estimated from the average recrystallized grain sizes and free dislocation densities, respectively.

grain size distribution (Fig. 3), leading to an underestimation of the mean recrystallized grain size and an overestimation of the stresses.

The stresses estimated using the ‘wet’ paleopiezometer of Jung & Karato (2001b) are similar to those obtained from the free dislocation density. For a wet dunite flow law and a strain rate of 10⁻¹⁴ s⁻¹, these rather high stresses are attained only just below the Moho and in the crust (Fig. 19). Strain rates of 10⁻¹³ s⁻¹ are needed to produce stresses of 20–60 MPa in a wet mantle. These results are consistent with the IR spectroscopy data which show that olivines in the studied samples have rather low water contents.

Evidence for fluid–melt percolation and consequences for the olivine microstructures and CPO

All coarse-grained Avacha xenoliths present clear microstructural evidence of reactive percolation of Si-rich fluids

leading to crystallization of orthopyroxene at the expense of olivine. This evidence includes the following: (1) large orthopyroxenes elongated parallel to the lineation enclosing small olivine grains in crystallographic continuity with neighbouring olivine crystals (Fig. 4a); (2) corrosion embayments in olivine crystals filled by interstitial orthopyroxenes that may show kink bands subparallel to the olivine subgrain walls or be undeformed (Fig. 4c); (3) concentration of interstitial orthopyroxenes in lenses parallel to the foliation (Figs 2a,b, 3 and 5). The latter observations also indicate that the reactive fluid percolation is synkinematic to the main high-temperature deformation. Concentration of interstitial orthopyroxenes in lenses parallel to the foliation may, for example, result from deformation-controlled fluid segregation, similar to melt segregation in simple shear experiments using olivine–spinel–basalt aggregates, where melt-rich bands tends to form parallel to the shear plane (Holtzman *et al.*, 2003).

On the other hand, the absence of intra-crystalline deformation features in most interstitial orthopyroxenes (Fig. 2g and 3b) or in small crystals filling corrosion embayments in olivine (Figs 3b and 4c), as well as the stronger dispersion of the orthopyroxene CPO relative to the olivine CPO (Fig. 6), implies that reactive fluid percolation probably continued after the deformation slowed down. Finally, because it led to orthopyroxene crystallization, the fluid percolation must have occurred at temperatures below the hydrous orthopyroxene solidus, which is 1360°C and 1270°C at 1 GPa and 2 GPa (Kushiro *et al.*, 1968), respectively. This is consistent with a fluid percolation occurring during the main deformation at the base of the lithosphere and/or in the shallow asthenosphere (Fig. 19).

Although olivine CPO patterns are rather homogeneous in the studied peridotites, the intensity of the CPO decreases with increasing volume fraction of fine-grained olivine crystals. Within a sample, the *J* index is 2–4 times lower for fine-grained olivine crystals than for coarse ones (Fig. 9). These fine-grained olivine crystals, which dominantly occur in opx-rich bands parallel to the foliation (Fig. 2b and e), are either undeformed or display deformation microstructures similar to the coarse olivine grains, such as subgrains or undulose extinction. Dynamic recrystallization may explain both the grain size reduction and the dispersion of the CPO. However, crystallographic continuity between neighbouring olivine crystals separated by interstitial orthopyroxene (Fig. 3) suggests that they were originally part of a single coarse olivine crystal. We propose that the dominant mechanism for olivine grain size reduction in these bands is the reactive percolation of Si-rich fluids leading to olivine replacement by orthopyroxene. A similar phenomenon has been described by Dijkstra *et al.* (2002) in the Othris peridotite massif (Greece).

Concentration of fluids or melts within the bands may have favoured the activation of diffusional processes and grain boundary sliding resulting in weaker olivine CPO. Similar weakening of the olivine CPO in deformation experiments on olivine–melt aggregates (Holtzman *et al.*, 2003) and in peridotite massifs where deformation occurred in the presence of small melt fractions (Dijkstra *et al.*, 2002; Le Roux *et al.*, 2008; Soustelle *et al.*, 2009) has also been attributed to an increased contribution of diffusion to deformation. Fluid concentration in these bands probably also resulted in a viscosity decrease (Holtzman & Kohlstedt, 2007) and, because the bands are aligned, in anisotropic mechanical behaviour where shearing parallel to the foliation is favoured.

Superimposed on the high-temperature deformation microstructures, the studied peridotites show a wide range of features related to melt or fluid transport in the lithospheric mantle. These features include the formation of

the acicular orthopyroxene aggregates (Fig. 4d), probably at the expense of pre-existing coarse orthopyroxene crystals, and the crystallization of a fine-grained ol–opx–oxides \pm cpx \pm amph \pm glass matrix (Fig. 2g) at the expense of orthopyroxene and olivine. The fine-grained matrix occurs as a pervasive film along grain boundaries (Figs 2e, g and 4c), in millimeter-scale lenses flattened parallel the foliation (Fig. 2d), or forming irregular pockets in equigranular peridotite AV16 (Fig. 2f). It corrodes olivine and orthopyroxene and crosscuts their internal deformation microstructures (Fig. 4c), implying post-deformation crystallization. In general, a higher concentration of the fine-grained matrix along grain boundaries is observed in the opx-rich bands. We propose that it records the higher permeability of these bands caused by their finer grain size (Wark & Watson, 2000; Le Roux *et al.*, 2008). The fine-grained matrix is also observed along anastomosing veinlets that crosscut large deformed olivine crystals (Fig. 4e). Acicular orthopyroxenes similar to those observed in the studied peridotites have been generally attributed to metasomatism by aqueous fluids with a small amount of dissolved silicates (Arai & Kida, 2000; Grégoire *et al.*, 2001, 2007; McInnes *et al.*, 2001; Arai *et al.*, 2003; Ishimaru *et al.*, 2007; Facer & Downes, 2008). However, the fine-grained matrix crystallizes at the expense of both olivine and orthopyroxene. Moreover, the acicular orthopyroxenes are not the sole reaction product; the fine-grained matrix also contains less common amphibole and clinopyroxene. Together these observations suggest that their formation is due instead to a reaction between harzburgite and a hydrous silicate melt.

The late-stage melt percolation likely took place under static lithospheric conditions and has no major influence on the olivine CPO unless it results in crystallization of large volumes of the fine-grained ol–opx–oxides \pm amph \pm cpx \pm glass matrix. It may also have contributed to the partial annealing of the deformation structures in the olivine in these bands. The fine-grained ol–opx–oxides \pm amph \pm cpx \pm glass matrix, which occurs in post-deformation veinlets crosscutting olivine crystals (Fig. 4d and e), often encloses polygonal olivine crystals free of dislocations and deformation microstructures (Figs 4f and 14c, f), which probably result from neo-crystallization of olivine. The fine-grained peridotite AV16 that is essentially composed of strain-free polygonal olivine crystals probably represents a highly fractured domain or the wall-rock of a major dyke. Its weak CPO ($J=1.98$) implies nevertheless that at least some of these strain-free polygonal olivines were inherited from coarser grains with a pre-existing and probably stronger CPO.

The observed microstructures suggest an evolution of the fluid transport process. It started by pervasive porous flow of Si-rich aqueous fluids synchronous with or following the high-temperature deformation (crystallization of

interstitial and coarse orthopyroxene at the expense of olivine). This was followed by porous flow of hydrous melts under static conditions (formation of the ol-opx-oxides \pm amph \pm cpx \pm glass matrix) that later evolved to melt transport localized in a network of connected veins formed by fluid-assisted fracturing. This variation in melt transport processes is consistent with the cooling history inferred from the orthopyroxene thermometry and from the deformation microstructures. It corroborates the inference of a continuous cooling history before extraction of the xenoliths from shallow lithospheric levels.

Hydration of the supra-subduction zone wedge mantle

Measurements of water concentrations in olivine and coarse orthopyroxene in the studied peridotites yield values between 1 and 8.6 ppm of H₂O by weight and 25 and 506 ppm of H₂O, respectively (Table 2). These are respectively lower and higher than the theoretical H₂O saturation values for olivine and orthopyroxene in spinel peridotites equilibrated between 1 and 2 GPa (16 and 290 ppm H₂O, Keppler & Bolfan-Casanova, 2006). Olivines in the studied peridotites are clearly water undersaturated; their water concentrations are 2–8 times lower than the theoretical calculated saturation value. Orthopyroxenes, on the other hand, have heterogeneous water contents ranging from 10 times lower to 1.7 times higher than the saturation value. Consequently, the orthopyroxene/olivine water concentration ratios in the studied xenoliths vary from 5 to 126. The extreme values differ significantly from the orthopyroxene/olivine water concentration ratio derived from the theoretical saturation values (\sim 18, Keppler & Bolfan-Casanova, 2006), from orthopyroxene/olivine water concentration ratios measured in natural spinel peridotites (40.7 ± 18.9 , Grant *et al.*, 2007; Falus *et al.*, 2008), or from partition coefficients ($D_{\text{water}}^{\text{opx/ol}}$) determined experimentally for peridotites equilibrated in the spinel field (7–10, Aubaud *et al.*, 2004). This suggests that olivines and orthopyroxenes in the Avacha peridotites are not in equilibrium with respect to their water contents.

Orthopyroxenes in the Avacha peridotites, except for coarse peridotite AV10, have lower water contents (25–218 ppm H₂O by weight) than the theoretical saturation value (290 ppm H₂O, Keppler & Bolfan-Casanova, 2006). The measured water contents in the three most hydrated pyroxenes (Table 2) are nevertheless in the same range as those observed in water saturation experiments on pure and natural enstatite at pressures of 1 and 2.5 GPa: 114 ± 10 and 238 ± 7 ppm H₂O by weight (Paterson calibration), respectively (Rauch & Keppler, 2002). If we calculate water concentration ratios between these pyroxenes and the coarser, more water-enriched olivines in each sample we obtain values of 27 in AV3, 31 in AV10 and 26 in AV15. These values are consistent with the

concentration ratios obtained in saturation experiments, suggesting that these three orthopyroxenes and the coarser olivine are in equilibrium and display water concentrations that could represent the original (pre-exhumation) water contents in our samples. The lowest water contents (25–55 ppm H₂O by weight) were measured in a coarse orthopyroxene from sample AV15 and in one acicular orthopyroxene from sample AV16. These two orthopyroxenes are texturally different, but both samples display wide fine-grained zones, which probably result from interaction with a percolating melt. Peslier *et al.* (2002) proposed that an increase in oxygen fugacity linked to percolation of metasomatic fluids or melts may account for observed low water concentrations in orthopyroxenes from subduction-related mantle xenoliths. Oxygen fugacity in Kamchatka peridotite xenoliths is between 0 and 2 Δ FMQ (fayalite-magnetite-quartz buffer) with a peak around +1 Δ FMQ (Arai *et al.*, 2003; Ionov *et al.*, 2007; Ionov, 2010), which corresponds to the values measured by Peslier *et al.* (2002). The high oxygen fugacity of the Kamchatka samples is also consistent with the fact that the major O–H absorption bands of the olivine IR spectrum are at 3354 and 3328 cm⁻¹ (Fig. 11, Berry *et al.*, 2005). Finally, extremely high water contents (>500 ppm H₂O by weight) were observed in one orthopyroxene from sample AV10. Such concentrations have been previously observed only under high-pressure conditions or in Al-rich orthopyroxene (Rauch & Keppler, 2002; Keppler & Bolfan-Casanova, 2006), yet the orthopyroxenes in our samples are equilibrated at low pressures (1–2 GPa) and have low Al₂O₃ contents (\leq 2 wt %). Although the absorbance spectrum is coherent (Fig. 16), we cannot completely discard the possibility of an analytical problem concerning this measurement. However, independently of this extreme value, the broad variations in orthopyroxene water contents, both within and between samples in the Kamchatka xenoliths, suggest that the H₂O concentration in minerals, particularly in orthopyroxene, is controlled by localized melt or fluid percolation, as a result of melt segregation during porous flow or in fractures.

Despite the fact that water concentrations in the Avacha olivines are within the range observed in other spinel-peridotite xenoliths from supra-subduction zone settings (Demouchy, 2004; Peslier & Luhr, 2006; Falus *et al.*, 2008), they are relatively low. A probable explanation is loss of water by diffusion to the host magma during the transport of the xenoliths (Demouchy *et al.*, 2006; Peslier & Luhr, 2006). The observation that small olivines have the lowest water concentrations is consistent with dehydration. Measurements in a coarse olivine crystal yielded a broad range of values within a single grain; however, the variation is within the uncertainty of the measurements (\pm 30%) as the water contents are very low. Moreover, core–rim measurements in crystal ol7 of sample AV15

gave water contents of 5 and 2.5 ppm H₂O by weight, respectively, corroborating potential dehydration during the ascent of the xenolith in the magma. The orthopyroxene, in contrast, has not experienced dehydration during the ascent of the xenoliths. Hence, we can use the water concentration in orthopyroxenes AV3opx1, AV10opx1 and AV15opx3 (Table 2), which have water contents in the range of those observed in water saturation experiments on pure and natural enstatite, and $D_{\text{water}}^{\text{opx/ol}}$ consistent with the data of Aubaud *et al.* (2004) to calculate a hypothetical concentration of water in olivine before the inferred dehydration. This yields values of 13–28 ppm H₂O by weight, which are consistent with the theoretical saturation value (16 ppm H₂O).

Experiments predict that incorporation of water in olivine results in activation of different slip systems (e.g. Jung & Karato, 2001a). Jung *et al.* (2006) show that the transition from dominant glide on (010)[100] to (001)[100] under high-temperature and moderate-stress conditions occurs at ~15 wt ppm H₂O. The low measured water contents in olivine (1–8.6 wt ppm H₂O) and stresses estimated from the various paleopiezometers (3–60 MPa) imply a dominant activation of the (010)[100] system. However, if dehydration occurred during the ascent of the xenoliths to the surface, olivine would have higher water contents, corresponding to the transition between dominant glide on the [100](010) and [100](001) systems. This is consistent with the CPO data, which imply that olivine deformed by [100] glide on both (010) and (001) planes.

Implications for the dynamics of the supra-subduction zone mantle

The analysis of the textures and deformation microstructures of the Avacha xenoliths allows us partially to reconstruct their thermo-mechanical history even if the precise timing of the different episodes cannot be established. The first recorded event is high-degree partial melting at shallow mantle depths (1–2 GPa, Ionov, 2009). This was followed by deformation under high-temperature, low-stress conditions, contemporaneous with porous flow of a hydrous melt or fluid. Cooling and integration of the samples into the lithosphere mark the end of the major deformation and result in a change of the melt–fluid transport process to fracturing. Finally, two samples (AV20 and AV21) were crosscut by orthopyroxenite veins of probably magmatic origin. This evolution can be compared with the long and complex history of the Kamchatka subduction zone.

High degrees of partial melting at shallow depths are observed only at mid-ocean ridges or in the mantle wedge above subduction zones. Based on the modal (absence of primary cpx and high orthopyroxene contents relative to olivine) and chemical compositions (Al–Fe relations) of

the Avacha peridotites, Ionov (2009) proposed that they are probably residues of hydrous melting in the mantle wedge. Numerical simulations by Arcay *et al.* (2007a, 2007b) show that influx of water and the resulting viscosity reduction in the mantle wedge may induce an upwelling of the lithosphere–asthenosphere boundary, allowing partial melting at depths shallower than 50 km. The Avacha peridotites may represent the residues of such a shallow partial melting process that were subsequently carried away by wedge convection, experiencing high-temperature, low-stress deformation and porous flow of hydrous fluids or melts at the base of the lithosphere and/or in the shallow asthenosphere.

The cooling recorded consistently by the change in deformation and fluid transport mechanisms and by the thermometry (Ionov, 2010) suggests that the Avacha peridotites were subsequently accreted to the lithosphere. To account for this evolution, we need to invoke a process producing a decrease in temperature in the mantle wedge and, hence, the deepening of the isotherms, leading to accretion of the shallow asthenospheric mantle to the lithosphere. Numerical models show that a decrease in the velocity of plate convergence reduces the convective vigour in the wedge, leading to a decrease in temperature in the mantle wedge and thickening of the upper plate (Arcay *et al.*, 2007b).

The present Kamchatka peninsula was formed by the collision of two volcanic arcs in response to the closure, between the late Miocene and the Quaternary, of a back-arc basin that separated two opposed subduction zones (Konstantinovskaia, 2001). A decrease in the convergence velocity associated with the collision of the two arcs may thus account for a decrease in the mantle wedge temperatures, leading to accretion of shallow asthenospheric mantle to the base of the lithosphere of the upper plate and cooling of the latter. This collision resulted in the eastward displacement of the volcanic front; calc-alkaline magmas from this new volcanic front fractured the lithosphere and carried to the surface the Avacha xenoliths that record both an asthenospheric and a lithospheric history.

CONCLUSION

Our observations show that although the spinel harburgite xenoliths from the Avacha volcano were extracted from the upper part of the lithospheric mantle (≥ 45 km), they record a thermo-mechanical history that started with partial melting and deformation under asthenospheric conditions, followed by accretion to the base of the lithosphere and subsequent cooling. Percolation of hydrous fluids or melts began in the asthenosphere and continued under lithospheric conditions. This succession of events, which suggests cooling of the supra-subduction zone mantle, is

consistent with the evolution of the Kamchatka arc since the late Miocene.

Percolation of small-fraction fluids or hydrated melts is recorded at all stages of the long history of the Avacha xenoliths. Analysis of the microstructures suggests that early ingress of Si-rich aqueous fluids was contemporaneous with deformation under high-temperature, low-stress conditions and took place essentially by reactive porous flow. Deformation-induced fluid segregation is probably responsible for the development of irregular compositional banding parallel to the foliation; higher degrees of interaction with fluids led to opx-enrichment and olivine grain size reduction by crystallization of orthopyroxene at the expense of olivine and to a local decrease in viscosity which, because the bands are aligned, result in anisotropic mechanical behaviour.

Olivine CPO shows clear axial [100] patterns that record deformation by dislocation creep with dominant activation of the high-temperature, low-stress, low-pressure $\{0kl\}[100]$ slip systems. This interpretation is consistent with the elongation of olivine crystals in the [100] directions and with the well-developed (100) tilt boundaries observed in the decorated sections and in EBSD maps. Olivine CPO within the opx-rich bands is similar, but more dispersed than the CPO in the neighbouring coarse domains. This suggests that the concentration of fluids in these bands does not result in a change in dominant olivine slip direction, but enhances the contribution of diffusional processes to the deformation.

Subsequent cooling and accretion to the lithosphere led to a continuous transition from reactive porous flow to the development of a network of interconnected veins and probably also to a change in the fluid composition towards hydrated melts. This later percolation produced crystallization of acicular orthopyroxene aggregates and of a fine-grained matrix composed of ol-opx-oxides \pm amph \pm cpx \pm glass at the expense of both orthopyroxene and olivine. Finally, the xenoliths were crosscut by veins and carried up to the surface by calc-alkaline magmas.

In spite of the microstructural evidence for interaction with hydrous fluids or melts at all stages of their supra-subduction zone evolution, the water contents in olivine are low (1–8.6 wt ppm). These values are nevertheless similar to those observed in spinel peridotites from various subduction zone settings. If these xenoliths have been dehydrated during their ascent, the maximum water content expected would be 13–28 wt ppm H₂O. This could explain the activation of both (010) and (001) slip planes in olivine. On the other hand, water contents in orthopyroxene are strongly variable (25–506 wt ppm H₂O), probably recording spatially heterogeneous interaction with fluids or melts and compositional disequilibrium.

ACKNOWLEDGEMENTS

We thank C. Nevado and D. Delmas, who supplied high-quality polished thin sections for EBDS measurement. FTIR analyses were performed at Université Montpellier 2 (France) with the help of David Maurin at the Laboratoire Colloids, Verre et Nanomatériaux, and at Université Blaise Pascal, Clermont-Ferrand (France) with the help of Nathalie Bolfan-Casanova at the Laboratoire Magmas et Volcans. D. Mainprice is thanked for discussions on the interpretation of dislocation structures, and for providing software for analysing and plotting CPO data. We acknowledge Arjan Dijkstra, Phil Skemer and Jessica Warren for their constructive reviews. This study was partially funded by the program SEDIT of the Institut National des Sciences de l'Univers (INSU-CNRS), France, in the frame of the project 'Deformation in the supra-subduction mantle' coordinated by A.T. V.S. benefited from a PhD scholarship from the Ministère de la Recherche et de l'Enseignement Supérieur.

REFERENCES

- Amelinckx, S. & Dekeyser, W. (1959). The structure and properties of grain boundaries. *Solid State Physics* **8**, 325–499.
- Arai, S. & Kida, M. (2000). Origin of fine-grained peridotite xenoliths from Iraya volcano of Batan Island, Philippines: deserpentinization or metasomatism at the wedge mantle beneath an incipient arc? *Island Arc* **9**(4), 458–471.
- Arai, S., Ishimaru, S. & Okrugin, V. (2003). Metasomatized harzburgite xenoliths from Avacha volcano as fragments of mantle wedge of the Kamchatka arc: Implication for the metasomatic agent. *Island Arc* **12**(2), 233–246.
- Arcay, D., Doin, M.-P., Tric, E., Bousquet, R. & de Capitani, C. (2006). Overriding plate thinning in subduction zones: Localized convection induced by slab dehydration. *Geochemistry, Geophysics, Geosystems* **7**(2), doi:10.1029/2005GC001061.
- Arcay, D., Doin, M.-P., Tric, E. & Bousquet, R. (2007a). Influence of the precollisional stage on subduction dynamics and the buried crust thermal state: Insights from the numerical simulations. *Tectonophysics* **441**, 27–45.
- Arcay, D., Tric, E. & Doin, M.-P. (2007b). Slab surface temperature in subduction zone: Influence of the interplate decoupling depth and upper mantle plate thinning processes. *Earth and Planetary Science Letters* **255**, 324–338.
- Aubaud, C., Hauri, E. H. & Hirschmann, M. M. (2004). Hydrogen partition coefficient between nominally anhydrous minerals and basaltic melts. *Geophysical Research Letters* **31**, L20611.
- Avdeiko, G. P., Popruzhenko, S. V. & Palueva, A. A. (2002). The tectonic evolution and volcano-tectonic zonation of the Kuril–Kamchatka island-arc system. *Geotectonics* **36**(4), 312–327.
- Avé-Lallemant, H. G. & Carter, N. L. (1970). Syntectonic recrystallization of olivine and modes of flow in the upper mantle. *Geological Society of America Bulletin* **81**, 2003–2020.
- Bai, Q., Mackwell, S. J. & Kohlstedt, D. L. (1991). High-temperature creep of olivine single-crystals. I. Mechanical results for buffered samples. *Journal of Geophysical Research—Solid Earth and Planets* **96**(B2), 2441–2463.
- Bell, D., Rossman, G. & Moore, R. (2004). Abundance and partitioning of OH in a high-pressure magmatic system: Megacrysts from

- the Monastery kimberlite, South Africa. *Journal of Petrology* **45**(8), 1539–1564.
- Bell, D. R., Rossman, G. R., Maldener, J., Endisch, D. & Rauch, F. (2003). Hydroxide in olivine: A quantitative determination of the absolute amount and calibration of the IR spectrum. *Journal of Geophysical Research—Solid Earth* **108**(B2), 2015.
- Bénard, A. & Ionov, D. A. (2009). Veined peridotite xenoliths from the Avacha volcano, Kamchatka: Fluid types and fluid–rock interaction in supra-subduction mantle. *Geochimica et Cosmochimica Acta* **73**, [13(S1)], A108.
- Ben Ismail, W. & Mainprice, D. (1998). An olivine fabric database: an overview of upper mantle fabrics and seismic anisotropy. *Tectonophysics* **296**, 145–158.
- Berry, A. J., Hermann, J., O'Neill, H. S. C. & Foran, G. J. (2005). Fingerprinting the water site in mantle olivine. *Geology* **33**(11), 869–872.
- Blacic, J. D. (1972). Effect of water on the experimental deformation of olivine. In: Heard, H. C., Borg, I. Y., Carter, N. L. & Rayleigh, C. B. (eds) *Flow and Fracture of Rocks*. American Geophysical Union: Washington, pp. 109–115.
- Bolfan-Casanova, N., Keppler, H. & Rubie, D. C. (2000). Water partitioning between nominally anhydrous minerals in the MgO–SiO₂–H₂O system up to 24 GPa: implications for the distribution of water in the Earth's mantle. *Earth and Planetary Science Letters* **182**(3–4), 209–221.
- Bouchez, J. L., Mainprice, D. H., Trepied, L. & Doukhan, J.-C. (1984). Secondary lineation in a high-T quartzite (Galicia, Spain): an explanation for an abnormal fabric. *Journal of Structural Geology* **6**(1/2), 159–165.
- Braitseva, O. A., Bazanova, L. I., Melekestev, I. V. & Sulerzhitskiy, L. D. (1998). Large Holocene eruptions of Avacha volcano, Kamchatka (7250–3700 ¹⁴C years B.P.). *Volcanology and Seismology* **20**, 1–27.
- Bunge, H. J. (1982). *Texture Analysis in Materials Sciences*. London: Butterworth.
- Byerlee, J. (1978). Friction of rocks. *Pure and Applied Geophysics* **116**(4–5), 615–626.
- Bystricky, M., Kunze, K., Burlini, L. & Burg, J. P. (2000). High shear strain of olivine aggregates; rheological and seismic consequences. *Science* **290**(5496), 1564–1567.
- Cagnioncle, A.-M., Parmentier, E. M. & Elkins-Tanton, L. T. (2007). Effect of solid flow above a subducting slab on water distribution and melting at convergent plate boundaries. *Journal of Geophysical Research* **112**, B09402.
- Chopra, P. N. & Paterson, M. S. (1981). The experimental deformation of dunite. *Tectonophysics* **78**(1–4), 453–473.
- Chopra, P. N. & Paterson, M. S. (1984). The role of water in the deformation of dunite. *Journal of Geophysical Research* **89**, 7861–7876.
- Costa, F. & Chakraborty, S. (2008). The effect of water on Si and O diffusion rates in olivine and implications for transport properties and processes in the upper mantle. *Physics of the Earth and Planetary Interiors* **166**, 11–29.
- Couvy, H., Frost, D. J., Heidelbach, F., Nyilas, K., Ungar, T., Mackwell, S. & Cordier, P. (2004). Shear deformation experiments of forsterite at 11 GPa–1400°C in the multianvil apparatus. *European Journal of Mineralogy* **16**(6), 877–889.
- Currie, C. A. & Hyndman, R. D. (2006). The thermal structure of subduction zone back arcs. *Journal of Geophysical Research* **111**(B8), B08404.
- Currie, C. A., Huismans, R. S. & Beaumont, C. (2008). Thinning of continental backarc lithosphere by flow-induced gravitational instability. *Earth and Planetary Science Letters* **269**, 436–447.
- Demouchy, S. (2004). Water in the Earth's interior: Thermodynamics and kinetics of hydrogen incorporation in olivine and wadsleyite. Universität Bayreuth.
- Demouchy, S., Jacobsen, S. D., Gaillard, F. & Stern, C. R. (2006). Rapid magma ascent recorded by water diffusion profiles in mantle olivine. *Geology* **34**(6), 429–432.
- Demouchy, S., Mackwell, S. J. & Kohlstedt, D. L. (2007). Influence of hydrogen on Fe–Mg interdiffusion in (Mg,Fe)O and implications for Earth's lower mantle. *Contributions to Mineralogy and Petrology* **154**, 279–289.
- Dijkstra, A. H., Drury, M. R., Vissers, R. L. M. & Newman, J. (2002). On the role of melt–rock reaction in mantle shear zone formation in the Othris Peridotite Massif (Greece). *Journal of Structural Geology* **24**(9), 1431–1450.
- Doukhan, J.-C., Doukhan, N., Naze, L. & Van Duysen, J.-C. (1986). Défauts de réseau et plasticité cristalline dans les pyroxènes: Une revue. *Bulletin de Minéralogie* **109**, 377–374.
- Durham, W. B., Goetze, C. & Blake, B. (1977). Plastic-flow of oriented single-crystals of olivine. 2. Observations and interpretation of dislocation-structures. *Journal of Geophysical Research* **82**(36), 5755–5770.
- Facer, J. & Downes, H. (2008). Hydrous fluid metasomatism in spinel dunite xenoliths from the Bearpaw Mountains, Montana, USA. *9th International Kimberlite Conference*. Frankfurt. Extended abstract No. 9IKC-A-00116.
- Falus, G., Tommasi, A., Ingrin, J. & Szabo, C. (2008). Deformation and seismic anisotropy of the lithospheric mantle in the southeastern Carpathians inferred from the study of mantle xenoliths. *Earth and Planetary Science Letters* **272**, 50–64.
- Frank, F. C. & Read, W. T. J. (1950). Multiplication processes for slow moving dislocations. *Physical Review* **79**, 722–723.
- Gerya, T. V. & Yuen, D. A. (2003). Rayleigh–Taylor instabilities from hydration and melting propel ‘cold plumes’ at subduction zones. *Earth and Planetary Science Letters* **212**, 47–62.
- Gorbatov, A., Kostoglodov, V., Suarez, G. & Gordeev, E. (1997). Seismicity and structure of the Kamchatka subduction zone. *Journal of Geophysical Research* **102**(B8), 17883–17898.
- Gorbatov, A., Dominguez, J., Suarez, G., Kostoglodov, V., Zhao, D. & Gordeev, E. (1999). Tomographic imaging of the P-wave velocity structure beneath the Kamchatka peninsula. *Geophysical Journal International* **137**, 269–279.
- Grant, K., Ingrin, J., Lorand, J. & Dumas, P. (2007). Water partitioning between mantle minerals from peridotite xenoliths. *Contributions to Mineralogy and Petrology* **154**(1), 15–34.
- Grégoire, M., McInnes, B. I. A. & O'Reilly, S. Y. (2001). Hydrous metasomatism of oceanic sub-arc mantle, Lihir, Papua New Guinea; Part 2. Trace element characteristics of slab-derived fluids. *Lithos* **59**(3), 91–108.
- Grégoire, M., Jego, S., Maury, R. C., Polve, M., Payote, B., Tamayo, R. A., Jr & Yumul, G.P., Jr (2007). Metasomatic interactions between slab-derived melts and depleted mantle: Insights from xenoliths within Monglo adakite (Luzon arc, Philippines). *Lithos* **103**(3–4), 415–430.
- Ham, R. K. (1961). The determination of dislocation densities in thin films. *Philosophical Magazine* **6**(69), 1183–1184.
- Hier-Majumder, S., Anderson, I. M. & Kohlstedt, D. L. (2004). Influence of proton on Fe–Mg interdiffusion in olivine. *Journal of Geophysical Research* **B2**, B02202.
- Hirsch, P. B., Howie, A., Nicholson, B. B. & Pashley, D. W. (1965). *Electron Microscopy of Thin Crystals*. London: Butterworth.
- Hirth, G. & Kohlstedt, D. L. (1995). Experimental constraints on the dynamics of the partially molten upper-mantle. 2. Deformation in the dislocation creep regime. *Journal of Geophysical Research—Solid Earth* **100**(B8), 15441–15449.

- Holtzman, B. K. & Kohlstedt, D. L. (2007). Stress-driven melt segregation and strain partitioning in partially molten rocks: Effects of stress and strain. *Journal of Petrology* **48**, 2379–2406.
- Holtzman, B. K., Groebner, N. J., Zimmerman, M. E., Ginsberg, S. B. & Kohlstedt, D. L. (2003). Stress-driven melt segregation in partially molten rocks. *Geochemistry, Geophysics, Geosystems* **4**, article number 8607.
- Honda, S., Saito, M. & Nakakuki, T. (2002). Possible existence of small-scale convection under the backarc. *Geophysical Research Letters* **29**(21), 2043, doi:10.1029/2002GL015853.
- Ionov, D. A. (2010). Petrology of Mantle Wedge Lithosphere: New Data on Supra-Subduction Zone Peridotite Xenoliths from the Andesitic Avacha Volcano, Kamchatka. *Journal of Petrology* **51**, 327–361.
- Ionov, D. A. & Seitz, H.-M. (2008). Lithium abundances and isotopic compositions in mantle xenoliths from subduction and intra-plate settings: Mantle sources vs. eruption histories. *Earth and Planetary Science Letters* **266**(3–4), 316–331.
- Ionov, D. A., Bruegmann, G., Seitz, H.-M., Lahaye, Y. & Woodland, A. B. (2007). Peridotite xenoliths from the andesitic Avacha volcano, Kamchatka—any signatures of subduction metasomatism? Abstracts, 17th Goldschmidt Conference, Cologne. *Geochemica et Cosmochimica Acta*, 71 [15(S1)], A430.
- Ishimaru, S., Arai, S., Ishida, Y., Shirasaka, M. & Okrugin, V. (2007). Melting and multi-stage metasomatism in the mantle wedge beneath a frontal arc inferred from highly depleted peridotite xenoliths from the Avacha volcano, Southern Kamchatka. *Journal of Petrology* **48**(2), 395–433.
- Jung, H. & Karato, S. (2001a). Water-induced fabric transitions in olivine. *Science* **293**(5534), 1460–1463.
- Jung, H. & Karato, S. I. (2001b). Effects of water on dynamically recrystallized grain-size of olivine. *Journal of Structural Geology* **23**(9), 1337–1344.
- Jung, H., Katayama, I., Jiang, Z., Hiraga, I. & Karato, S. (2006). Effect of water and stress on the lattice-preferred orientation of olivine. *Tectonophysics* **421**(1–2), 1–22.
- Karato, S. (1989). Grain growth kinetics in olivine aggregates. *Tectonophysics* **168**, 255–273.
- Karato, S., Toriumi, M. & Fujii, T. (1980). Dynamic recrystallization of olivine single crystals during high temperature creep. *Geophysical Research Letters* **7**(9), 649–652.
- Karato, S. I., Paterson, M. S. & Fitz Gerald, J. D. (1986). Rheology of synthetic olivine aggregates—influence of grain-size and water. *Journal of Geophysical Research—Solid Earth and Planets* **91**(B8), 8151–8176.
- Karato, S., Rubie, D. C. & Yan, H. (1993). Dislocation recovery in olivine under deep upper mantle conditions—Implications for creep and diffusion. *Journal of Geophysical Research* **20**(5), 315–322.
- Katayama, I., Jung, H. & Karato, S. I. (2004). New type of olivine fabric from deformation experiments at modest water content and low stress. *Geology* **32**(12), 1045–1048.
- Keppler, H. & Bolfan-Casanova, N. (2006). Thermodynamics of water solubility and partitioning. In: Keppler, H. & Smyth, J. R. (eds) *Water in Nominally Anhydrous Minerals*. Geochemical Society, Mineralogical Society of America: Washington, pp. 193–230.
- Kharakhin, V. V. (1996). Tectonics and history of sedimentary basins development. In: Rodnikov, A. G., Tuezov, I. K. & Kharakhin, V. V. (eds) *Structure and Dynamics of the Lithosphere and Asthenosphere of the Okhotsk Sea Region*. Moscow: Russian Academy of Science: Moscow, pp. 256–305.
- Kohlstedt, D. L. & Goetze, C. (1974). Low-stress high-temperature creep in olivine single-crystals. *Journal of Geophysical Research* **79**(14), 2045–2051.
- Kohlstedt, D. L., Goetze, C. & Durham, W. B. (1976a). Experimental deformation of single crystal olivine with application to flow in the mantle. In: Strens, R. G. J. (ed.) *The Physics and Chemistry of Minerals and Rocks*. Chichester: John Wiley, pp. 39–45.
- Kohlstedt, D. L., Goetze, C., Durham, W. B. & Vandersande, J. (1976b). New technique for decorating dislocations in olivine. *Science* **191**(4231), 1045–1046.
- Kohlstedt, D. L., Keppler, H. & Rubie, D. C. (1996). Solubility of water in the alpha, beta and gamma phases of (Mg,Fe)₂SiO₄. *Contributions to Mineralogy and Petrology* **123**(4), 345–357.
- Konstantinovskaia, E. A. (2001). Arc-continent collision and subduction reversal in the Cenozoic evolution of the Northwest Pacific: an example from Kamchatka (NE Russia). *Tectonophysics* **333**(1–2), 75–94.
- Kushiro, I., Yöder, H. S. J. & Nishikawa, N. (1968). Effect of water on the melting of enstatite. *Geological Society of America Bulletin* **79**(12), 1685–1692.
- Lee, C. A. (2003). Compositional variation of density and seismic velocities in natural peridotites at STP conditions: Implications for seismic imaging of compositional heterogeneities in the upper mantle. *Journal of Geophysical Research* **108**(B9), 2444.
- Le Roux, V., Bodinier, J.-L., Tömmasi, A., Alard, O., Dautria, J.-M., Vauchez, A. & Riches, A. J. V. (2007). The Lherz spinel lherzolite: Refertilized rather than pristine mantle. *Earth and Planetary Science Letters* **259**, 599–612.
- Le Roux, V., Tömmasi, A. & Vauchez, A. (2008). Feedback between melt percolation and deformation in an exhumed lithosphere–asthenosphere boundary. *Earth and Planetary Science Letters* **274**, 401–413.
- Levin, V., Park, J., Brandon, M., Lees, J., Peyton, V., Gordeev, E. & Ozerov, A. (2002). Crust and upper mantle of Kamchatka teleseismic receiver functions. *Tectonophysics* **358**, 233–253.
- Levin, V., Droznin, D., Park, J. & Gordeev, E. (2004). Detailed mapping of seismic anisotropy with local shear waves in southeastern Kamchatka. *Geophysical Journal International* **158**, 1009–1023.
- Mackwell, S. J. (1991). High-temperature rheology of enstatite: implications for creep in the mantle. *Geophysical Research Letters* **18**(11), 2027–2030.
- Mackwell, S. J., Kohlstedt, D. L. & Paterson, M. S. (1985). The role of water in the deformation of olivine single-crystals. *Journal of Geophysical Research—Solid Earth and Planets* **90**(NB13), 1319–1333.
- Manea, V. C., Manea, M., Kostoglodov, V. & Sewell, G. (2005). Thermal models, magma transport and velocity anomaly estimation beneath southern Kamchatka. In: Foulger, G., Natland, J. & Presnall, D. (eds) *Plates, Plumes and Paradigms*. Geological Society of America, Special Papers.
- McInnes, B. I. A., Gregoire, M., Binns, R. A., Herzig, P. M. & Hannington, M. D. (2001). Hydrous metasomatism of oceanic sub-arc mantle, Lihir, Papua New Guinea: petrology and geochemistry of fluid-metasomatised mantle wedge xenoliths. *Earth and Planetary Science Letters* **188**(1–2), 169–183.
- Mei, S. & Kohlstedt, D. L. (2000a). Influence of water on plastic deformation of olivine aggregates 1. Diffusion creep regime. *Journal of Geophysical Research—Solid Earth* **105**(B9), 21457–21469.
- Mei, S. & Kohlstedt, D. L. (2000b). Influence of water on plastic deformation of olivine aggregates 2. Dislocation creep regime. *Journal of Geophysical Research—Solid Earth* **105**(B9), 21471–21481.
- Mei, S., Bai, W., Hiraga, T. & Kohlstedt, D. L. (2002). Influence of melt on the creep behavior of olivine–basalt aggregates under hydrous conditions. *Earth and Planetary Science Letters* **201**(3–4), 491–507.

- Mercier, J. C. C., Anderson, D. A. & Carter, N. L. (1977). Stress in lithosphere—*inferences from steady-state flow of rocks*. *Pure and Applied Geophysics* **115**(1–2), 199–226.
- Miller, G. H., Rossman, G. R. & Harlow, G. E. (1987). The natural occurrence of hydroxide in olivine. *Physics and Chemistry of Minerals* **14**(5), 461–472.
- Nicolas, A. & Poirier, J. P. (1976). *Crystalline Plasticity and Solid State Flow in Metamorphic Rocks*. London: John Wiley.
- Paterson, M. S. (1982). The determination of hydroxyl by infrared absorption in quartz, silicate-glasses and similar materials. *Bulletin de Minéralogie* **105**(1), 20–29.
- Peslier, A. & Luhr, J. (2006). Hydrogen loss from olivines in mantle xenoliths from Simcoe (USA) and Mexico: Mafic alkalic magma ascent rates and water budget of the sub-continental lithosphere. *Earth and Planetary Science Letters* **242**(3–4), 302–319.
- Peslier, A. H., Luhr, J. F. & Post, J. (2002). Low water contents in pyroxenes from spinel-peridotites of the oxidized, sub-arc mantle wedge. *Earth and Planetary Science Letters* **201**(1R), 69–86.
- Peyton, V., Levin, V., Park, J., Brandon, M., Lees, J., Gordeev, E., Ozerov & A., (2001). Mantle flow at a slab edge: seismic anisotropy in the Kamchatka region. *Geophysical Research Letters* **28**(2), 379–382.
- Philpotts, A. R. (1990). *Principles of Igneous and Metamorphic Rocks*. Englewood Cliffs, NJ: Prentice Hall.
- Poirier, J. P. (1985). *Creep of Crystals. High-temperature Deformation Processes in Metals, Ceramics and Minerals*. Cambridge: Cambridge University Press.
- Raleigh, C. B. & Kirby, S. H. (1970). Creep in the upper mantle. *Mineralogical Society of America, Special Papers* **3**, 113–121.
- Ranalli, G. (1995). *Rheology of the Earth*, 2nd edn. London: Chapman & Hall.
- Raterron, P., Chen, J., Li, L., Weidner, D. & Cordier, P. (2007). Pressure-induced slip-system transition in forsterite: Single-crystal rheological properties at mantle pressure and temperature. *American Mineralogist* **92**(8–9), 1436–1445.
- Rauch, M. & Keppler, H. (2002). Water solubility in orthopyroxene. *Contributions to Mineralogy and Petrology* **143**(5), 525–536.
- Skemer, P., Katayama, I., Zhenting, J. & Karato, S. (2005). The misorientation index: Development of a new method for calculating the strength of lattice-preferred orientation. *Tectonophysics* **411**, 157–167.
- Soustelle, V., Tommasi, A., Bodinier, J.-L., Garrido, C. J. & Vauchez, A. (2009). Deformation and reactive melt transport in the mantle lithosphere above a large-scale partial melting domain: the Ronda peridotite massif, S Spain. *Journal of Petrology* **50**(7), 1335–1266.
- Tatsumi, Y., Furukawa, Y., Kogiso, T., Yamanaka, Y., Yokoyama, T. & Fedotov, S. A. (1994). A 3rd volcanic chain in Kamchatka—thermal anomaly at transform convergence plate boundary. *Geophysical Research Letters* **21**(7), 537–540.
- Tommasi, A., Tikoff, B. & Vauchez, A. (1999). Upper mantle tectonics: three-dimensional deformation, olivine crystallographic fabrics and seismic properties. *Earth and Planetary Science Letters* **168**(1–2), 173–186.
- Tommasi, A., Mainprice, D., Canova, G. & Chastel, Y. (2000). Viscoplastic self-consistent and equilibrium-based modeling of olivine lattice preferred orientations: Implications for the upper mantle seismic anisotropy. *Journal of Geophysical Research—Solid Earth* **105**(B4), 7893–7908.
- Tommasi, A., Gibert, B., Seipold, U. & Mainprice, D. (2001). Anisotropy of thermal diffusivity in the upper mantle. *Nature* **411**(6839), 783–786.
- Tommasi, A., Godard, M., Coromina, G., Dautria, J. M. & Barszczus, H. (2004). Seismic anisotropy and compositionally induced velocity anomalies in the lithosphere above mantle plumes: a petrological and microstructural study of mantle xenoliths from French Polynesia. *Earth and Planetary Science Letters* **227**(3–4), 539–556.
- Tommasi, A., Vauchez, A., Godard, M. & Belley, F. (2006). Deformation and melt transport in a highly depleted peridotite massif from the Canadian Cordillera: Implications to seismic anisotropy above subduction zones. *Earth and Planetary Science Letters* **252**, 245–259.
- Tommasi, A., Vauchez, A. & Ionov, D. A. (2008). Deformation, static recrystallization, and reactive melt transport in shallow subcontinental mantle xenoliths (Tök Cenozoic volcanic field, SE Siberia). *Earth and Planetary Science Letters* **272**, 65–77.
- Van der Wal, D., Chopra, P., Drury, M. & Gerald, J. F. (1993). Relationships between dynamically recrystallized grain-size and deformation conditions in experimentally deformed olivine rocks. *Geophysical Research Letters* **20**(14), 1479–1482.
- Vauchez, A. & Garrido, C. J. (2001). Seismic properties of an asthenospherized lithospheric mantle: constraints from lattice preferred orientations in peridotite from the Ronda massif. *Earth and Planetary Science Letters* **192**(2), 235–249.
- Vollmer, F. W. (1990). An application of eigenvalue methods to structural domain analysis. *Geological Society of America Bulletin* **102**, 786–791.
- Wark, D. A. & Watson, B. E. (2000). Effect of grain size on the distribution and transport of deep-seated fluids and melts. *Geophysical Research Letters* **27**(14), 2029–2032.
- Zhang, S. & Karato, S.-I. (1995). Lattice preferred orientation of olivine aggregates deformed in simple shear. *Nature* **375**, 774–777.
- Zhang, S., Karato, S.-I., Fitz Gerald, J., Faul, U. H. & Zhou, Y. (2000). Simple shear deformation of olivine aggregates. *Tectonophysics* **316**, 133–152.
- Zhuravlev, A. V. & Antipov, M. P. (1993). The Okhotsk sea area of Cenozoic submergence. In: Sokolov, B. S. (ed.) *Seismostratigraphic Researches in Eurasia*. Moscow: Nauka, pp. 160–183.
- Zimmerman, M. E. & Kohlstedt, D. L. (2004). Rheological properties of partially molten lherzolite. *Journal of Petrology* **45**(2), 275–298.